The Pennsylvania State University

The Graduate School

Department of Electrical Engineering

ELECTROMAGNETIC MODELING OF NANOWIRES AND OPTICAL NANOANTENNAS

A Thesis in

Electrical Engineering

by

Brian William Rybicki

Submitted in Partial Fulfillment
of the Requirements
for the Degree of

Master of Science

August 2008

The thesis of Brian William Rybicki was reviewed and approved* by the following:

Douglas H. Werner
Professor of Electrical Engineering
Thesis Advisor

Ping L. Werner
Professor of Electrical Engineering

W. Kenneth Jenkins
Professor of Electrical Engineering
Head of the Department of Electrical Engineering

*Signatures are on file in the Graduate School

ABSTRACT

Both the fabrication and placement of nanostructures (i.e. structures whose dimensions are on the order of nanometers) has matured to the point where antenna- and waveguide-like elements may be manufactured and precisely placed into useful configurations. This is of particular interest because it extends conventional antenna concepts and applications into the terahertz and even optical regimes. To support these inquiries, it is necessary to correctly describe the electromagnetic properties with proper modeling. This thesis will address a few specific topics in the modeling of nanoscale electromagnetics and novel applications at terahertz and optical frequencies. First, an analytical treatment of the scattering from GaP nanowires and asymptotic forms of the average internal intensities are derived. The ratio of orthogonally polarized intensities with a vanishingly thin nanowire confirms the presence of the 'antenna effect' in this limit. The simulation of arrays of metallic nanowires shows that they may function well as frequency selective surfaces in the mid-infrared. By introducing a small gap in each nanowire, large near fields are produced at resonance that may find use in field enhanced spectroscopy. The excitation of nanowires allows them to function as optical nanoantennas and they are well described by conventional antenna parameters such as input impedance, radiation efficiency and directivity. Nanoantennas can be simulated more efficiently by taking advantage of the surface impedance condition, though with less accurate calculation of the input reactance.

TABLE OF CONTENTS

LIST OF FIGURES

LIST OF TABLES

ACKNOWLEDGEMENTS

I would like to thank my research advisers, Drs. Doug and Ping Werner for taking me on, first as an honors student and then in graduate school, and also for guiding me through the rigors of academia. My former instructor, honors adviser, and continual friend Jack Mitchell has been a strong presence and constant source of advice and encouragement. I have also cherished lunchtime discussions with Do-Hoon Kwon on the importance of career goals and the broader impact research may have. Finally, I cannot quantify how much the support of friends and family has helped me to reach the point I am at today. They have been truly great to me.

Chapter 1

Introduction

1.1 Motivation

Research in electromagnetics can be driven and directed by many different processes. Sometimes advances in theory push for the design, fabrication and experimentation of new and novel structures. In other cases, developments made in the production of innovative structures pull for better analytical or numerical modeling of their observed properties. One example of the latter is the recent interest in nanoscale electromagnetics. Both the fabrication and placement of nanostructures (i.e. structures whose dimensions are on the order of nanometers) has matured to the point where antenna- and waveguide-like elements may be manufactured and precisely placed into useful configurations. This is of particular interest because it extends conventional antenna concepts and applications into the terahertz and even optical regimes. Nanowires may be viewed as wire dipole elements, nanocones as broadband biconicals and nanotubes as circular waveguides. Recent work by Engheta suggests even the basic building blocks of circuits may have similar analogues [1].

To support these inquiries, it is necessary to correctly describe the electromagnetic properties with proper modeling. This thesis will address a few specific topics in the modeling of nanoscale electromagnetics and novel applications at terahertz and optical frequencies.

1.2 Analysis Methods

For the purpose of this work I will assume that the electromagnetic properties of a given material can be completely described by the bulk constitutive parameters μ and ε, which, although complex and frequency dependent, are isotropic and homogenous. Also, the materials will generally be nonmagnetic so the permeability is equal to its free space value ($\mu=\mu_0$). With this in mind, the vast majority of nanoscale electromagnetics can be described using mostly canonical EM methods. These fall into the very general categories of *analytical* and *numerical.* In either case the formulation may be exact or approximate.

1.2.1 Analytical

An analytical approach to a problem in electromagnetics seeks to find a closed form solution to the quantity of interest. The notion of "closed form" can mean a finite set of elementary functions or an infinite series of special functions. Even for deceivingly simple geometries, it can be very tedious to find an exact analytical solution. This usually depends on the separability of the Helmholtz equation in a particular coordinate system. The coordinate system is typically chosen to correspond to some symmetry of the problem. Therefore, we see exact solutions when considering simple shapes like spheres, infinite cylinders and planar half spaces (and also more exotic shapes like biconicals, spheroids and ellipsoids). Unfortunately, this severely limits the type of problems we can solve.

While it is rare to find an exact sphere or an infinite cylinder in a laboratory settting, the closed form solutions generated by analytical methods usually represent a

good approximation to some real problems. One example is the Raman scattering from long nanowires [2],[3],[4],[5]. Even though the nanowires are of finite extent, both the aspect ratio and electrical length are large enough that experimental results match well with the modal solution. The full analytical solution may not even be necessary in some instances because all but the lowest orders terms are negligible. In fact, in certain limiting or asymptotic cases the solution may simplify significantly and lend much more physical insight than in endless summations of functions and coefficients.

1.2.2 Numerical

The full-wave approach in electromagnetics uses numerical techniques to solve specifically formulated equations. These equations can directly depend on the field quantities or they can be auxiliary in nature. The name "full-wave" distinguishes this technique from some approximate methods, such as ray tracing, in that the full wave characteristics from Maxwell's equations are accounted for. Another important distinction, one of great relevance here, is the accuracy of the formulation. An exact formulation will give the greatest accuracy; however, it may also require significant computational resources. Certain approximate formulations are much easier to solve. In some cases the reduction in accuracy from using an approximate formulation is more than offset by the increase in computation speed. This is, of course, very dependent on the type of problem.

Most full-wave approaches utilize a perfect electric conductor (PEC) boundary condition in their formulation. The only electric current considered is a surface current

flowing just along the outside of the boundary. This simplifies the formulation greatly and is good approximation to real metals at most radio and microwave frequencies. At infrared and optical frequencies metals behave as very poor conductors. Current can actually flow within the material, similar to a lossy dielectric. The exact formulation to this problem discretizes the full volume of material. This discretization must be fine enough to resolve both the skin depth of the metal (due to loss) and also the dispersion (due to the change in wavelength). The dielectric functions of metals are high enough that standard meshing guidelines (say $\lambda_{eff}/20$) result in very dense meshes. CPU time and memory are sacrificed for accuracy. One approximate formulation uses a surface impedance condition. In this approach impenetrability is restored to the material (i.e. no currents or fields allowed inside) and the surface current is modulated by an impedance that depends on the material parameters and geometry. Physically, currents and fields are present inside the metal, but their influence depends on the frequency range. The main advantages of this formulation are its computational efficiency and ease of integration into standard wire kernels [5].

1.3 Material Models

One important assumption inherent to the analysis methods above is that the bulk constitutive parameters are known. They can be determined from underlying physical models or from experimental data. Direct experimental data would seem to be the most desirable; however, it is often unavailable, incomplete or difficult to measure. Arbitrary analytical functions can be blindly fit to data points, but it is better if the model relates to

the underlying physics involved. Since the materials are nonmagnetic, the quantity of interest for modeling is the complex relative permittivity, often separated into real and imaginary parts,

$$\varepsilon_r = \varepsilon_r' - j\varepsilon_r'' . \tag{1-1}$$

The real part of the permittivity relates to the storage of electric energy while the imaginary part relates to the dissipation of electric energy.

The simplest model is the *Debye* model shown below,

$$\varepsilon_r(\omega) = \varepsilon_{r\infty} + \frac{\varepsilon_{rs} - \varepsilon_{r\infty}}{1 + j\omega\tau} . \tag{1-2}$$

This single pole model represents the frequency dependence as a relaxation between the high frequency value, $\varepsilon_{r\infty}$, and the dc or electrostatic value, ε_{rs}. In most cases $\varepsilon_{r\infty} = 1$. The relaxation time constant is given by τ. This model is most useful describing materials with permanent dipole moments such as polar liquids [6].

A more useful model, especially for insulators, is the *Lorentz* model, given as

$$\varepsilon_r(\omega) = \varepsilon_{r\infty} + \frac{\omega_p^2}{(\omega_0^2 - \omega^2) + j\omega\gamma} . \tag{1-3}$$

This model comes from an oscillator description of induced dipoles within a material and their response to an alternating field. The resonant frequency of the oscillator is ω_0, which represents the point of maximum real energy. The dampening constant, γ, introduces loss into the system. There is also a constant, ω_p, which defines the plasma frequency within the material.

The *Drude* model (1-4) is a surprisingly simple and accurate description of the behavior in conductors and doped semiconductors. It has been fit to measurements on

noble metals throughout the IR [7] and also to doped semiconductors at millimeter wavelengths [8].

$$\varepsilon_r(\omega) = \varepsilon_{r\infty} - \frac{\omega_p^2}{\omega^2 - j\omega\gamma} \tag{1-4}$$

The equation is very similar to the Lorentz model except the resonant frequency is taken to be at dc (set to zero), which describes the response of a free electron gas or plasma. Note the real part of the permittivity, ε_r', is negative for all frequencies below ω_p.

A hybrid model, such as the *Lorentz-Drude* model (1-5), offers a more complete description of metals at upper terahertz and optical frequencies [6],[9].

$$\varepsilon_r(\omega) = \varepsilon_{r\infty} - \frac{\omega_{p0}^2}{\omega^2 - j\omega\gamma_0} + \sum_n \frac{\omega_{pn}^2}{(\omega_n^2 - \omega^2) + j\omega\gamma_n} \tag{1-5}$$

The permittivity is composed a Drude term and superposition of Lorentz functions at resonant frequency ω_n and damping constant γ_n. At lower frequencies (well below to near the plasma frequency), the Drude term dominates while dielectric-like Lorentzian resonances become important from the observed plasma frequency and upwards.

1.4 Applications

Besides a topic for experimentation, nanowires and other nanoscale structures have garnered much interest for several potential applications. One of these is as an infrared frequency selective surface (FSS) [10],[11],[12],[13]. Arranged in a periodic array, nanowire segments essentially act as a scaled down dipole FSS. At resonance the

array reflects a large majority of the incident radiation. This resonance can be tailored in wavelength (frequency) to many different locations in the mid-IR, including several important atmospheric windows (3-5 μm and 8-12 μm). Laser cavities, beam splitters and polarizers could all benefit from this application, which avoids the need to stack many thin-film layers.

Another novel application for arrays of nanowires is as a substrate for harmful agent detection, surface enhanced Raman scattering (SERS) and other types of field enhanced spectroscopy [14],[15],[16],[17],[18]. This takes advantage of the large electric near field values produced at corners, along edges and, especially, within gaps ('Lightning rod effect'). In the context of SERS, these enhanced fields increase the returned signal at approximately $|E|^4$ [19]. At these enhancement factors we can even examine the structure of single molecules.

Possibly the most exciting area to develop around nanostructures is the creation of optical antennas. To those in the optics community, this is intriguing because it allows the confinement of light to areas much smaller than the incident wavelength [20]**.** Electrical engineers, on the other hand, see a plethora of analogs to devices common in the antenna and microwave fields. These include the development of nanocircuit elements [1], optical Yagi-Uda antennas [21], solar rectennas, and even optical near field probing [22]. Before these concepts can be properly applied at optical frequencies, it is necessary to characterize optical nanoantennas in terms of conventional antenna parameters. These include efficiency, input impedance and field pattern/directivity.

1.5 Summary

This thesis will begin with an analytical treatment of the scattering from long Gallium Phosphide nanowires in Chapter 2. The internal electrical field distribution, intensity per unit length and intensity polarization ratio will be examined. In addition, asymptotic forms of the intensity will be developed to give physical insight into the 'antenna effect' described in [3] and [4]**.** Chapter 3 will examine the spectrum from doubly periodic arrays of metallic nanowires with the goal of designing a bandstop IR FSS. The enhanced fields around tightly coupled regions will also be explored. Chapter 4 will characterize nanowires acting as optical antennas. This will include a discussion of conventional antenna parameters applied to nanoantennas, and the approximate (surface impedance) and exact (full volume discretization) modeling approaches.

Chapter 2

Asymptotic Scattering from Long, Single Nanowires

2.1 Motivation

In the Raman spectroscopy of semiconducting nanowires, there exists an angular dependence on the scattering intensities absent in bulk material [3],[4],[5]. Below a critical diameter this dependence closely follows a dipole pattern. We obtain a better explanation for this 'antenna effect' by considering the scattering from and average internal intensities within an infinite, right, circular cylinder. Even though the nanowires are of finite extent, the length-to-diameter ratios are considered sufficiently high (~100-700) that this is a valid approach [2]. The antenna effect is most prevalent when the transverse magnetic (TM) intensity dominates over the transverse electric (TE) intensity. In order to simplify the expressions and measure validity at small radii, we will apply asymptotic methods.

2.2 Permittivity of GaP

As mentioned in Section 1.3, it is absolutely vital that the material parameters are known in the region of interest. Fortunately, measured data exists for Gallium Phosphide (GaP) and is given in Fig. 2-1. The data has also been fit to a multiple Lorentizan model through a Particle Swarm Optimization [24]. This allowed the authors to produce a time

domain representation of the material dispersion. Since the following analysis assumes time-harmonic quantities, such a model will be unnecessary here.

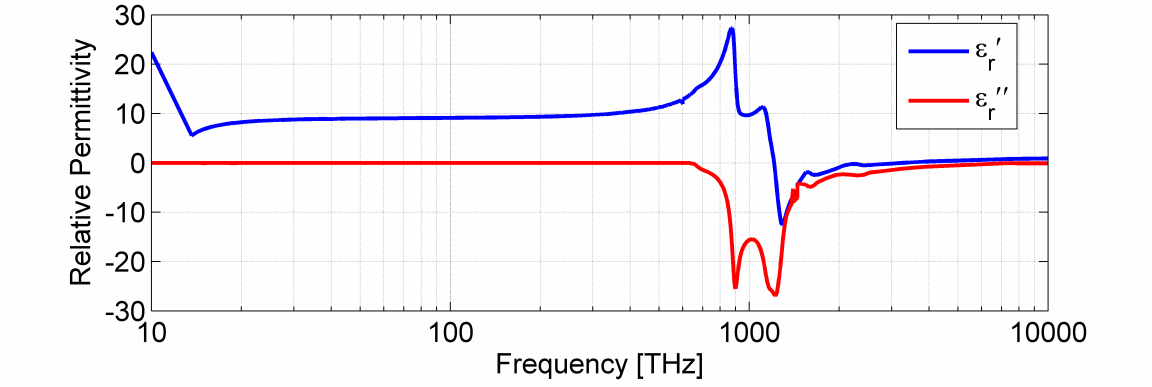

Fig. 2-1: The relative permittivity of GaP from 10 to 10^4 THz.

2.3 Example: Rayleigh Scattering from a Sphere

To illustrate how complicated formulas may be simplified greatly by the application of asymptotic approximations, consider the scattering from a dielectric sphere of radius, a, and relative permittivity, ε_r. The exact scattered field expressions involve several complicated summations of associated Legendre functions and spherical Bessel functions (see [25] or [26] for a complete treatment). When the sphere is small in terms of the incident wavelength (i.e. $k_0 a << 1$ where k_0 is the free space wavenumber), the series truncates and only the principal mode (zeroth order term) dominates. This leads to a compact expression for the far-zone scattered field,

$$E^s \simeq E_0 \frac{e^{-jkr}}{k_0 r}\left(\frac{\varepsilon_r - 1}{\varepsilon_r + 2}\right)(k_0 a)^3 . \qquad (2\text{-}1)$$

The backscatter cross section, σ_{BCS}, is given by

$$\sigma_{BCS} \simeq 4\pi a^2 \left(\frac{\varepsilon_r - 1}{\varepsilon_r + 2} \right)^2 (k_0 a)^4 . \qquad (2\text{-}2)$$

Note that there is a large resonance when $\varepsilon_r = -2$. For Drude (1-4) spheres in free space, this corresponds to the *Fröhlich frequency* [7], which is

$$\omega_F = \frac{\omega_p}{\sqrt{3}}, \text{ for } \gamma^2 \ll \omega_p^2 . \qquad (2\text{-}3)$$

Given an accepted set of measured permittivity data for silver [8], Fig. 2-2 compares the normalized backscatter cross section from silver, perfect dielectric and PEC spheres of a = 30 nm. This example shows the need to properly characterize materials at optical frequencies; the behavior of a "real metal" differs substantially from either ideal case.

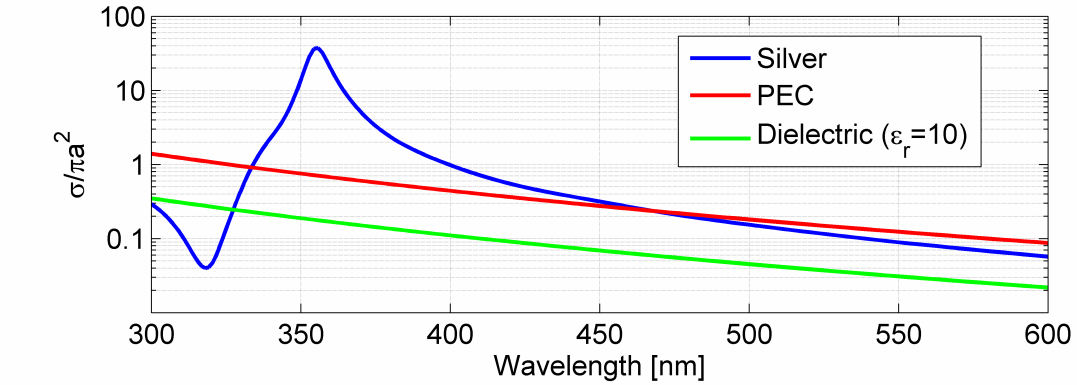

Fig. 2-2: Normalized backscatter cross section from a single sphere of a = 30 nm in Rayleigh approximation (2-2).

2.4 Derivation of Fields

Now let us briefly examine the scattered fields from an infinite circular cylinder by a normally incident plane wave. By separating the problem into two linearly independent polarizations, transverse magnetic (TM) and transverse electric (TE), we may avoid the use of vector harmonics [7] and focus on scalar expansions instead. This the preferred approach in [25] and [26].

2.4.1 TM Case

The plane wave is polarized along the cylinder (z) axis and incident normally as in Fig. 2-3.

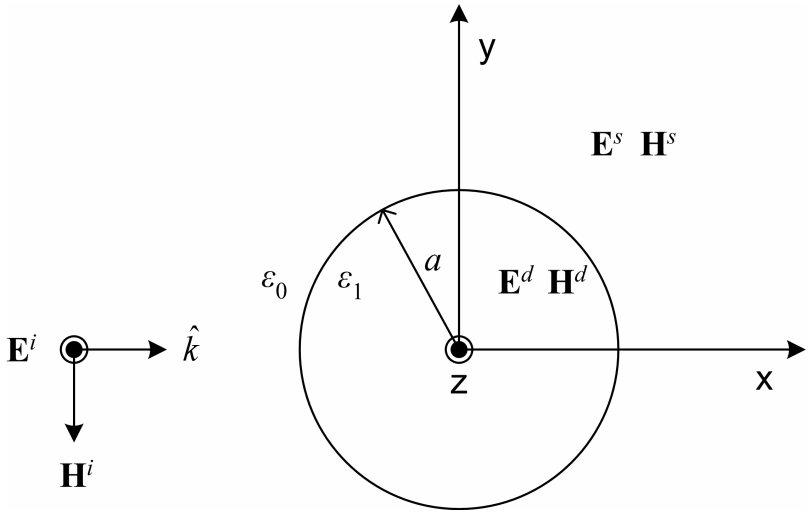

Fig. 2-3: TM wave incident on cross section of infinite dielectric cylinder

Assume the electric fields are separable into incident, scattered and dielectric components given in standard cylindrical coordinates by

$$\mathbf{E}^i = E_z^i \hat{z} = E_0 \sum_{n=-\infty}^{\infty} (-j)^n J_n(k_0\rho) e^{jn\varphi}\ \hat{z} \tag{2-4}$$

$$\mathbf{E}^s = E_z^s \hat{z} = E_0 \sum_{n=-\infty}^{\infty} (-j)^n a_n^{TM} H_n^{(2)}(k_0\rho) e^{jn\varphi}\ \hat{z} \tag{2-5}$$

$$\mathbf{E}^d = E_z^d \hat{z} = E_0 \sum_{n=-\infty}^{\infty} (-j)^n \left[b_n^{TM} J_n(k_1\rho) + c_n^{TM} Y_n(k_1\rho) \right] e^{jn\varphi}\ \hat{z} \tag{2-6}$$

with the usual notation for Bessel and Hankel functions. Notice the electric fields have only one vector component for this polarization. The magnetic field is related by Faraday's Law,

$$\mathbf{H} = -\frac{1}{j\omega\mu} \nabla \times \mathbf{E} = -\frac{1}{j\omega\mu} \left(\frac{1}{\rho} \frac{\partial E_z}{\partial \varphi} \hat{\rho} - \frac{\partial E_z}{\partial \rho} \hat{\varphi} \right), \tag{2-7}$$

and has two vector components orthogonal to the electric field.

The unknown coefficients a_n, b_n and c_n are found by enforcing continuity on the tangential electric and magnetic fields at the cylinder surface. They are [26]

$$a_n^{TM} = \frac{J_n'(k_0 a) J_n(k_1 a) - \sqrt{\varepsilon_r} J_n'(k_1 a) J_n(k_0 a)}{\sqrt{\varepsilon_r} J_n'(k_1 a) H_n^{(2)}(k_0 a) - J_n(k_1 a) H_n^{(2)\prime}(k_0 a)} \tag{2-8}$$

$$b_n^{TM} = \frac{J_n(k_0 a) H_n^{(2)\prime}(k_1 a) - J_n'(k_0 a) H_n^{(2)}(k_0 a)}{J_n(k_1 a) H_n^{(2)\prime}(k_0 a) - \sqrt{\varepsilon_r} J_n'(k_1 a) H_n^{(2)}(k_0 a)} \tag{2-9}$$

$$c_n^{TM} = 0\,. \tag{2-10}$$

For nanowires with electrically small radii, these coefficients can be simplified by using the following small argument approximations ($|ka|<<1$) to the Bessel and Hankel functions [7],

$$J_0(x) \simeq 1 - \left(\frac{x}{2}\right)^2 \Rightarrow J_0'(x) \simeq -\frac{x}{2} + \frac{1}{2}\left(\frac{x}{2}\right)^3 \tag{2-11}$$

$$H_0^{(2)}(x) \simeq 1 - \left(\frac{x}{2}\right)^2 - j\frac{2}{\pi}\ln\left(\frac{x}{2}\right) \Rightarrow H_0^{(2)\prime}(x) \simeq -\frac{x}{2} + \frac{1}{2}\left(\frac{x}{2}\right)^3 - j\frac{2}{\pi x} \tag{2-12}$$

for $n = 0$ terms and

$$J_1(x) \simeq \frac{x}{2} - \frac{1}{2}\left(\frac{x}{2}\right)^3 \Rightarrow J_1'(x) \simeq \frac{1}{2} - \frac{3}{4}\left(\frac{x}{2}\right)^2 \tag{2-13}$$

$$H_1^{(2)}(x) \simeq \frac{x}{2} - \frac{1}{2}\left(\frac{x}{2}\right)^3 + j\frac{2}{\pi x} \Rightarrow H_1^{(2)\prime}(x) \simeq \frac{1}{2} - \frac{3}{4}\left(\frac{x}{2}\right)^2 - j\frac{2}{\pi x^2} \tag{2-14}$$

for $n = 1$ terms. This leads to approximate expressions for the internal and scattered field coefficients,

$$a_0^{TM} \simeq -j\pi\left(\varepsilon_r - 1\right)\left(\frac{k_0 a}{2}\right)^2 \tag{2-15}$$

$$b_0^{TM} \simeq 1 - 2\left(\varepsilon_r - 1\right)\left(\frac{k_0 a}{2}\right)^2 \ln\left(\frac{k_0 a}{2}\right). \tag{2-16}$$

The above coefficients are accurate to $(k_0 a)^2$. It is easy to see that as the dielectric constant of the wire approaches the value of free space, the coefficients reach appropriate values (zero for scattering terms and one for transmitted terms). A comparison of the accuracy of these terms is given in Fig. 2-4. There is good agreement for radii less than 20 nm, which corresponds to $k_0 a \leq 0.26$ at a wavelength of 488 nm.

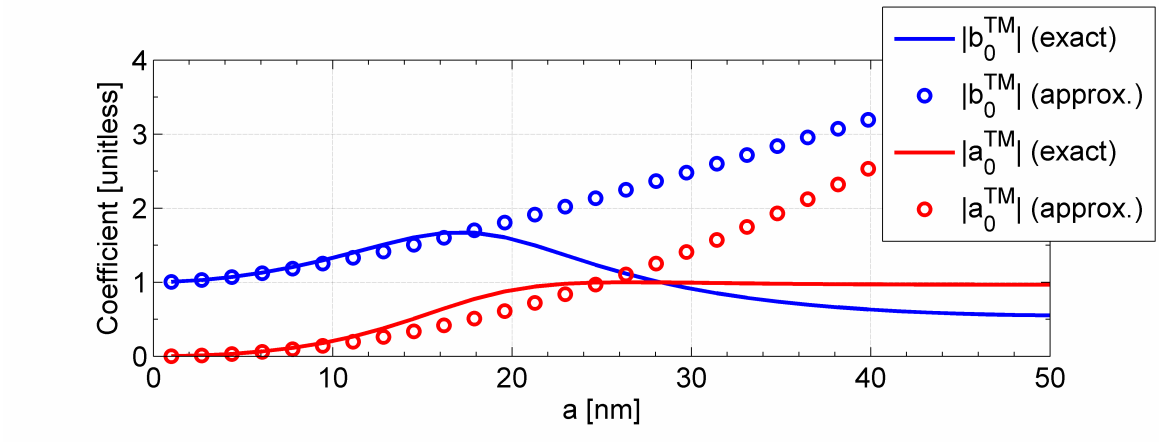

Fig. 2-4: Approximate and exact expressions of scattering coefficients for different radii (TM).

We may now develop an approximate equation for the scattered far field by taking the zeroth order term from (2-5) and applying the asymptotic formula

$$\lim_{|x|\to\infty} H_n^{(2)}(x) \simeq \sqrt{\frac{2j}{\pi}}(j)^n \frac{e^{-jx}}{\sqrt{x}} \tag{2-17}$$

to get

$$E_z^s \simeq E_0\sqrt{2j\pi}(\varepsilon_r - 1)\left(\frac{k_0 a}{2}\right)^2 \frac{e^{-jk_0\rho}}{\sqrt{k_0\rho}}. \tag{2-18}$$

The internal field, in the small radius limit, is found using an identical procedure to give

$$E_z^d \simeq E_0\left\{1 - 2\left(\varepsilon_r - 1\right)\left(\frac{k_0 a}{2}\right)^2 \ln\left(\frac{k_0 a}{2}\right)\right\}. \tag{2-19}$$

Note that (2-19) is constant over the nanowire cross-section. This is expected because the incident wavelength is large compared with the radius.

In Fig. 2-5 the fields of an a = 10 nm GaP nanowire are calculated by the full series given in (2-6) yet are nearly constant across the nanowire cross section. This confirms the uniformity predicted by (2-19) for small a. At larger radii, as shown in Fig. 2-6, there is much more variation in the internal fields. The approximation (2-19) is no longer valid.

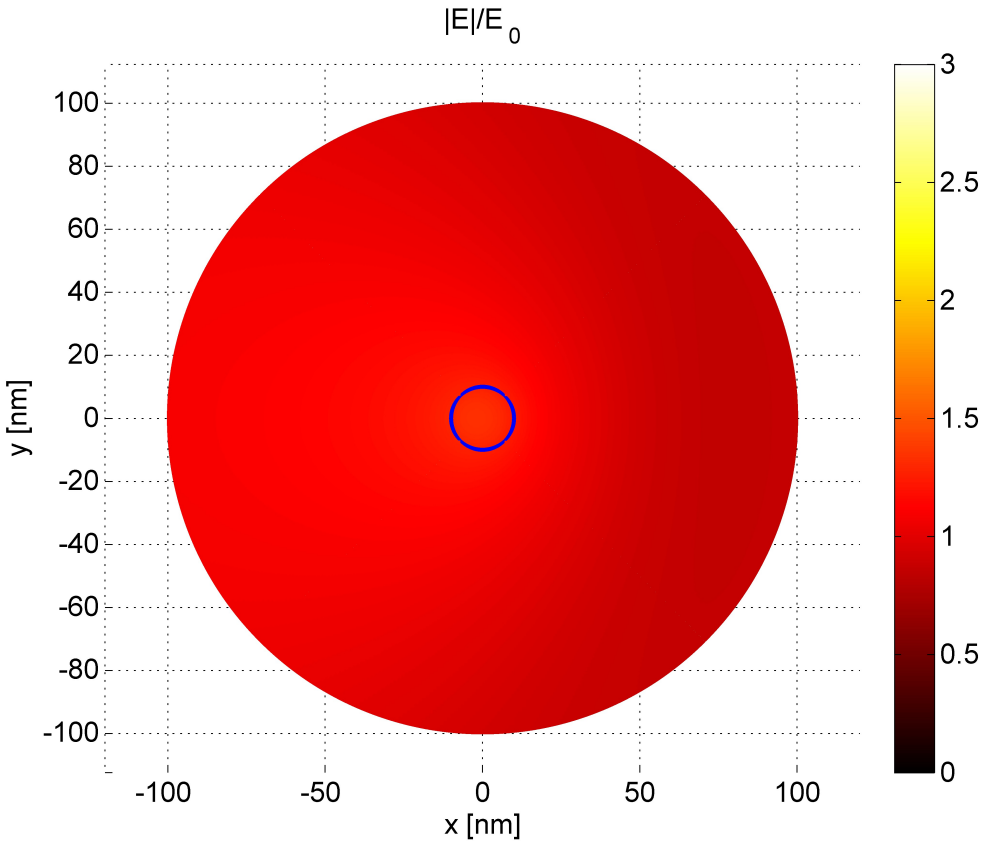

Fig. 2-5: Normalized field magnitude distribution from a TM^z plane wave scattering from an a = 10 nm GaP nanowire at λ_0 = 488 nm. The blue circle represents the material boundary.

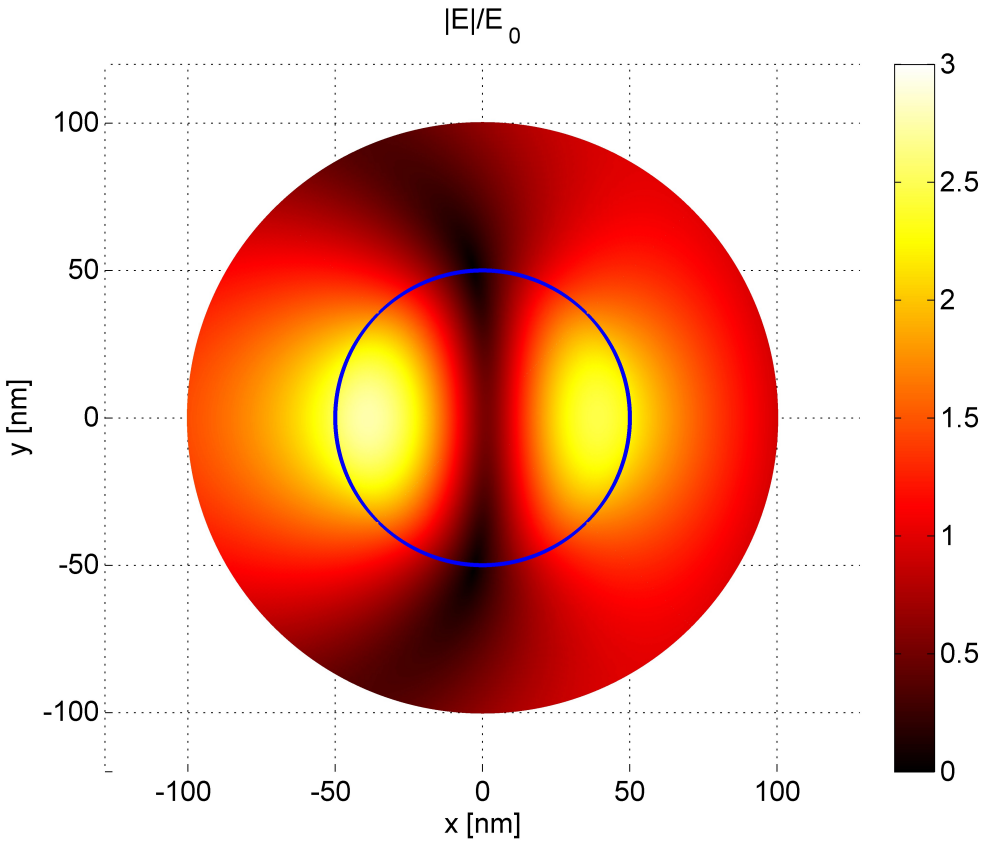

Fig. 2-6: Normalized field magnitude distribution from a TM^z plane wave scattering from an a = 50 nm GaP nanowire at λ_0 = 488 nm. The blue circle represents the material boundary.

2.4.2 TE Case

The incident wave is now assumed to be transverse electric as in Fig. 2-7.

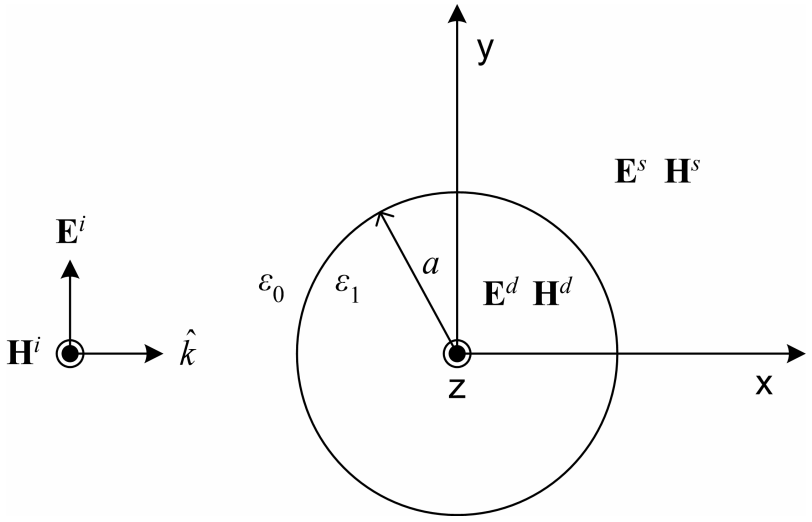

Fig. 2-7: TE wave incident on cross section of infinite dielectric cylinder

The resulting incident, scattered and dielectric magnetic field components are

$$\mathbf{H}^i = H_z^i \hat{z} = \frac{E_0}{\eta_0} \sum_{n=-\infty}^{\infty} (-j)^n J_n(k_0\rho) e^{jn\varphi}\ \hat{z} \tag{2-20}$$

$$\mathbf{H}^s = H_z^s \hat{z} = \frac{E_0}{\eta_0} \sum_{n=-\infty}^{\infty} (-j)^n a_n^{TE} H_n^{(2)}(k_0\rho) e^{jn\varphi}\ \hat{z} \tag{2-21}$$

$$\mathbf{H}^d = H_z^d \hat{z} = \frac{E_0}{\eta_0} \sum_{n=-\infty}^{\infty} (-j)^n \left[b_n^{TE} J_n(k_1\rho) + c_n^{TE} Y_n(k_1\rho) \right] e^{jn\varphi}\ \hat{z} \tag{2-22}$$

In this case the magnetic field has only one vector component while the electric field has two components in general. These are found from the application of Ampere's law

$$\mathbf{E} = \frac{1}{j\omega\varepsilon} \nabla \times \mathbf{H} = \frac{1}{j\omega\varepsilon} \left(\frac{1}{\rho} \frac{\partial H_z}{\partial \varphi} \hat{\rho} - \frac{\partial H_z}{\partial \rho} \hat{\varphi} \right). \tag{2-23}$$

The same boundary condition procedure as above is used to find the coefficients. The results are very similar to TM incidence with a slight change in the location of ε_r.

$$a_n^{TE} = \frac{J_n'(k_0a)J_n(k_1a) - \frac{1}{\sqrt{\varepsilon_r}} J_n'(k_1a)J_n(k_0a)}{\frac{1}{\sqrt{\varepsilon_r}} J_n'(k_1a)H_n^{(2)}(k_0a) - J_n(k_1a)H_n^{(2)\prime}(k_0a)} \tag{2-24}$$

$$b_n^{TE} = \frac{J_n(k_0a)H_n^{(2)\prime}(k_0a) - J_n'(k_0a)H_n^{(2)}(k_0a)}{J_n(k_1a)H_n^{(2)\prime}(k_0a) - \frac{1}{\sqrt{\varepsilon_r}} J_n'(k_1a)H_n^{(2)}(k_0a)} \tag{2-25}$$

$$c_n^{TE} = 0 \tag{2-26}$$

Similar approximate expressions can be developed for small radii ($|ka|<<1$) as in the TM polarization. In this case, however, both the first and zeroth order terms are important in the series. The additional small argument formulas (2-13) and (2-14) are needed to calculate these terms.

After much manipulation, in the limit $|ka|<<1$ the zeroth order coefficients reduce to

$$a_0^{TE} \simeq -j\pi \frac{(\varepsilon_r - 1)}{2} \left(\frac{k_0 a}{2} \right)^4 \tag{2-27}$$

$$b_0^{TE} \simeq 1 - (\varepsilon_r - 1) \left(\frac{k_0 a}{2} \right)^4 \ln\left(\frac{k_0 a}{2} \right) \tag{2-28}$$

while the first order coefficients become

$$a_1^{TE} \simeq -j\pi \left(\frac{\varepsilon_r - 1}{\varepsilon_r + 1} \right) \left(\frac{k_0 a}{2} \right)^2 \tag{2-29}$$

$$b_1^{TE} \simeq 2 \frac{\sqrt{\varepsilon_r}}{\varepsilon_r + 1}. \tag{2-30}$$

Similar to the TM polarization, Fig. 2-8 shows the convergence of the approximate and exact scattering coefficients as $a \to 0$. There is also good agreement for $a \leq 20$ nm.

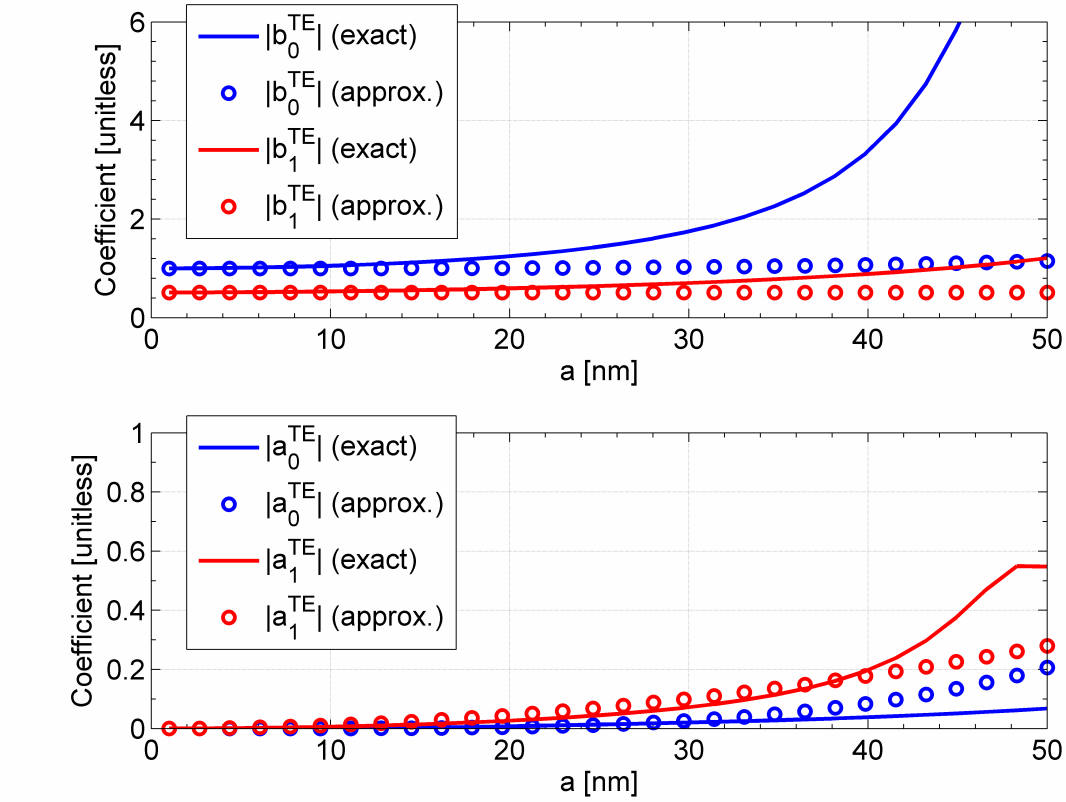

Fig. 2-8: Approximate and exact expressions of scattering coefficients for different radii (TE).

The far-zone scattered magnetic field, correct to quadratic order, is

$$H_z^s \simeq 2\sqrt{-2\pi j}\,\frac{E_0}{\eta_0}\left(\frac{\varepsilon_r - 1}{\varepsilon_r + 1}\right)\left(\frac{k_0 a}{2}\right)^2 \cos\varphi \frac{e^{-jk_0\rho}}{\sqrt{k_0\rho}}. \tag{2-31}$$

Applying (2-23) leads to the scattered electric field

$$\mathbf{E}^s \simeq \frac{2E_0\sqrt{-2\pi j}}{j\omega\varepsilon_0\eta_0\rho}\left(\frac{\varepsilon_r - 1}{\varepsilon_r + 1}\right)\left(\frac{k_0 a}{2}\right)^2 \frac{e^{-jk_0\rho}}{\sqrt{k_0\rho}}\left(jk_0\rho\cos\varphi\ \hat{\varphi} - \sin\varphi\ \hat{\rho}\right). \tag{2-32}$$

Similarly, the internal magnetic field is approximately

$$H_z^d \simeq \frac{E_0}{\eta_0}\left[1 - 4j\frac{\sqrt{\varepsilon_r}}{\varepsilon_r + 1}\left(\frac{k_1\rho}{2}\right)\cos\varphi\right] \tag{2-33}$$

while the internal electric field approaches

$$\mathbf{E}^d \simeq \frac{2E_0}{\varepsilon_r + 1}\hat{y}\,. \tag{2-34}$$

Again, terms higher than quadratic order are ignored in these field expressions. Similar to Rayleigh scattering from a dielectric sphere, there is a resonance for this polarization when $\varepsilon_r = -1$.

Fig. 2-9 confirms the constant nature of the internal electric fields at small radii. Note that the field is discontinuous at the material boundary because the polarization of the electric field is no longer tangential to the nanowire. An example of larger nanowire behavior is given in Fig. 2-10. Once again there is enough field variation in this case to preclude the use of (2-34).

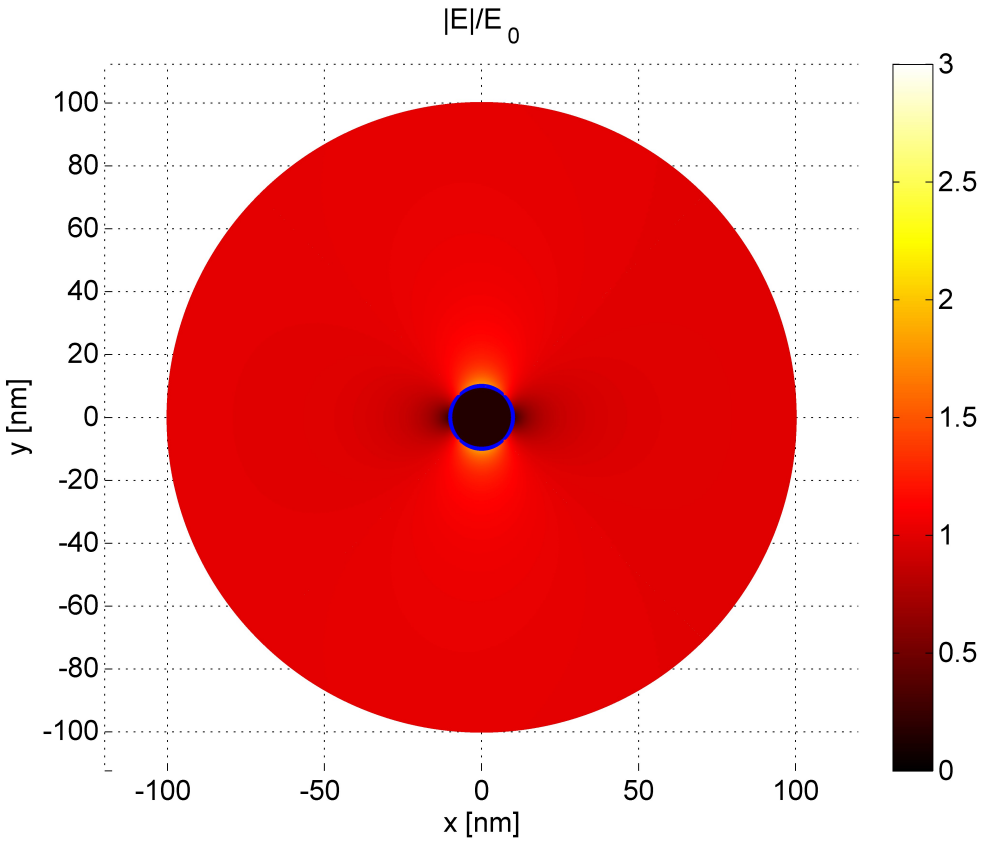

Fig. 2-9: Normalized field magnitude distribution from a TE^z plane wave scattering from an a = 10 nm GaP nanowire at λ_0 = 488 nm. The blue circle represents the material boundary.

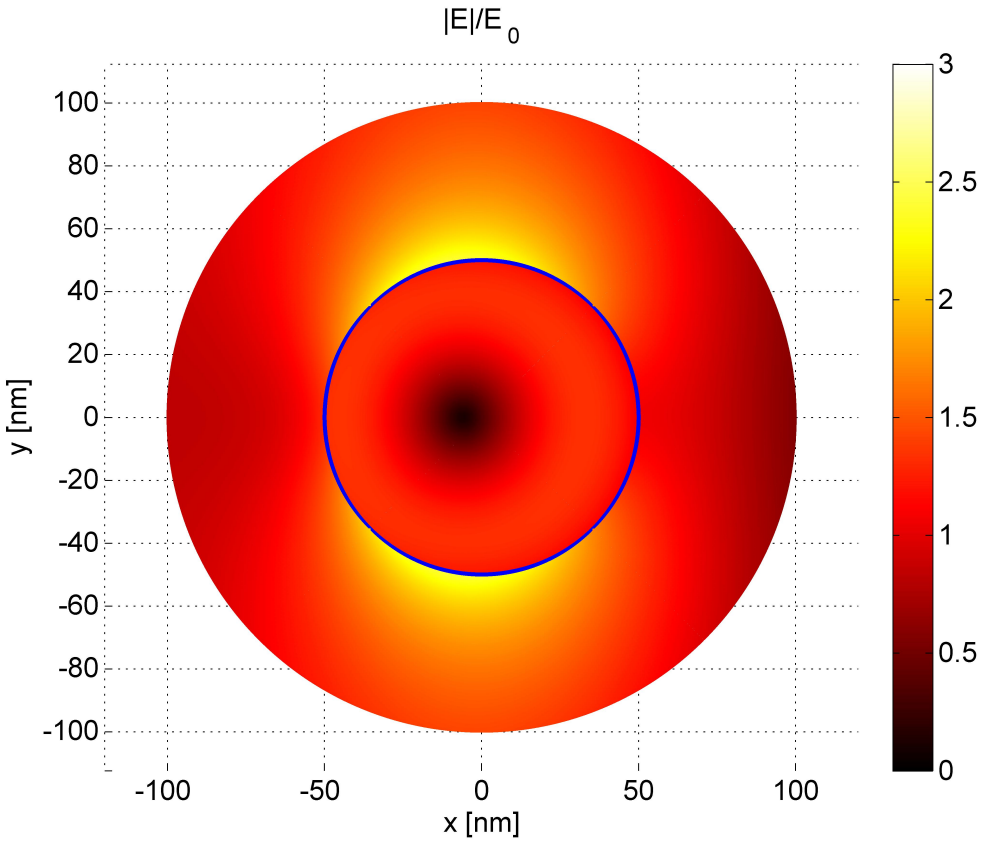

Fig. 2-10: Normalized field magnitude distribution from a TE^z plane wave scattering from an a = 50 nm GaP nanowire at λ_0 = 488 nm. The blue circle represents the material boundary.

2.5 Derivation of Average Internal Intensities

Besides field quantities, the average internal electric field intensity is also of interest in Raman scattering because the ratio of orthogonally polarized intensities predicts the antenna effect. Each intensity is given by the following integral [5],

$$I^{TM,TE} = \frac{1}{\pi a^2}\int_0^a\int_0^{2\pi} \left|\mathbf{E}^{TM,TE}\right|^2 \rho \, d\rho d\varphi . \tag{2-35}$$

Upon substitution of the appropriate field expressions, (2-35) may be integrated by a lengthy procedure described in [27] for either polarization.

2.5.1 TM Case

The resulting expression for the TM incidence internal field intensity is

$$I^{TM} = 2\left|E_0\right|^2 \sum_{n=-\infty}^{\infty} \left|b_n^{TM}\right|^2 \left[\frac{k_1 a\, J_{n+1}(k_1 a) J_n(k_1^* a) - k_1^* a\, J_n(k_1 a) J_{n+1}(k_1^* a)}{(k_1 a)^2 - (k_1^* a)^2}\right] \tag{2-36}$$

This equation diverges when loss in the material becomes negligible ($\varepsilon'' \approx 0$, $k_1^* \approx k_1$), therefore the following reformulation may be necessary

$$I^{TM} = \left| E_0 \right|^2 \sum_{n=-\infty}^{\infty} \left|b_n^{TM}\right|^2 \left[\left(J_n(k_1 a)\right)^2 - J_{n-1}(k_1 a) J_{n+1}(k_1 a)\right] \tag{2-37}$$

As shown previously for TM field expressions, the zeroth ($n = 0$) order term in the intensity series dominates at smaller radii ($|k_0 a| \to 0$). We may then isolate this term, apply the Bessel asymptotic expressions of (2-11) and (2-13), and substitute the approximate coefficient (2-16). This results in

$$I^{TM} \simeq |E_0|^2 \left| 1 - 2(\varepsilon_r - 1)\left(\frac{k_0 a}{2}\right)^2 \ln\left(\frac{k_0 a}{2}\right) \right|^2 \tag{2-38}$$

for complex permittivity and

$$I^{TM} \simeq |E_0|^2 \left[1 - 2(\varepsilon_r - 1)\left(\frac{k_0 a}{2}\right)^2 \ln\left(\frac{k_0 a}{2}\right) \right]^2 \left[1 + \varepsilon_r \left(\frac{k_0 a}{2}\right)^2 \right] \tag{2-39}$$

for real permittivity. Notice there is additional $(k_0 a)^2$ dependence in (2-39), whereas this term cancels in the derivation of (2-38).

Fig. 2-11 shows a comparison between the exact and approximate methods. Both approximate expressions converge to the exact intensity for $a \leq 15$ nm ($k_0 a \leq 0.19$ at a wavelength of 488 nm). Beyond these radii, the approximate expressions are not very accurate.

2.5.2 TE Case

In the case of TE incidence, the integral (2-35) becomes

$$I^{TE} = \frac{|E_0|^2}{|\varepsilon_r| \left[(k_1 a)^2 - (k_1^* a)^2 \right]} \sum_{n=-\infty}^{\infty} \left| b_n^{TE} \right|^2 \Big\{ (k_1 a) J_n(k_1 a) J_{n-1}(k_1^* a)$$

$$- (k_1^* a) J_{n-1}(k_1 a) J_n(k_1^* a) + (k_1 a) J_{n+2}(k_1 a) J_{n+1}(k_1^* a) - (k_1^* a) J_{n+1}(k_1 a) J_{n+2}(k_1^* a) \Big\} \tag{2-40}$$

for complex permittivity and

$$I^{TE} = \frac{|E_0|^2}{2\varepsilon_r} \sum_{n=-\infty}^{\infty} \left| b_n^{TE} \right|^2 \Big\{ \big(J_{n-1}(k_1 a)\big)^2 + \big(J_{n+1}(k_1 a)\big)^2 - J_n(k_1 a) \big[J_{n-2}(k_1 a) + J_{n+2}(k_1 a) \big] \Big\}$$

(2-41)

for real permittivity.

Unlike the TM case, first order ($|n| = 1$) terms cannot be neglected. Asymptotic forms may be found by following a procedure similar to that above with the additional first order terms included. After some arithmetic manipulation, this gives

$$I^{TE} \simeq \left|E_0\right|^2 \left\{ \frac{1}{4}\left(\frac{k_0 a}{2}\right)^2 + \frac{4}{\left|\varepsilon_r + 1\right|^2}\left[1 + \frac{\left|\varepsilon_r\right|^2}{12}\left(\frac{k_0 a}{2}\right)^4\right]\right\} \tag{2-42}$$

from (2-40) and

$$I^{TE} \simeq \left|E_0\right|^2 \left\{ \frac{1}{2}\left(\frac{k_0 a}{2}\right)^2 + \frac{4}{\left(\varepsilon_r + 1\right)^2}\left[1 - \varepsilon_r\left(\frac{k_0 a}{2}\right)^2\right]\right\} \tag{2-43}$$

from (2-41).

Examining Fig. 2-12, both exact intensity curves are nearly collinear for these small radii and at this polarization. Therefore, it is not surprising that the lossy and lossless approximations are similar to one another because they approximate equivalent expressions.

At infinitesimal radii ($a \to 0$), the ratio of intensities becomes

$$\frac{I^{TM}}{I^{TE}} \simeq \frac{\left|\varepsilon_r + 1\right|^2}{4} \tag{2-44}$$

which equals 50.7 for GaP at 488 nm. We may therefore conclude the antenna effect is present in nanowires with small to infinitesimal radii.

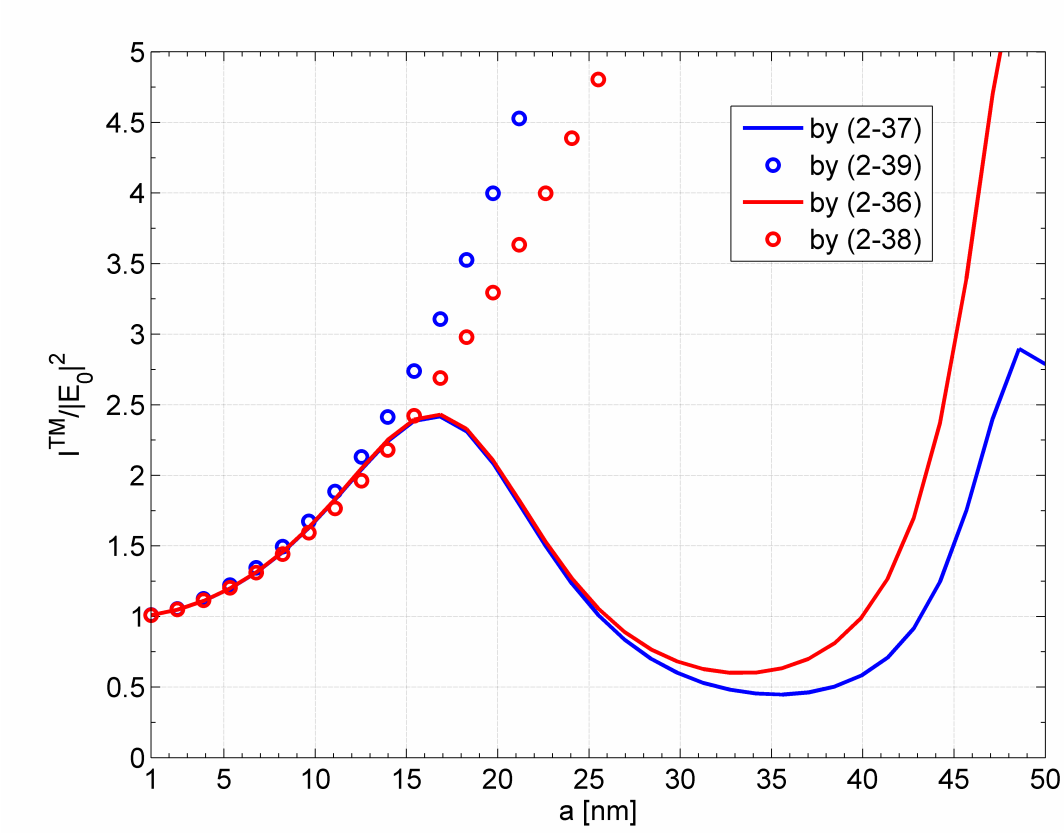

Fig. 2-11: Normalized average internal intensity in GaP nanowire, TM incidence at λ = 488 nm. Lossless expressions (blue) evaluated with $\varepsilon'' = 0$, lossy (red) with $\varepsilon'' = 0.0003$.

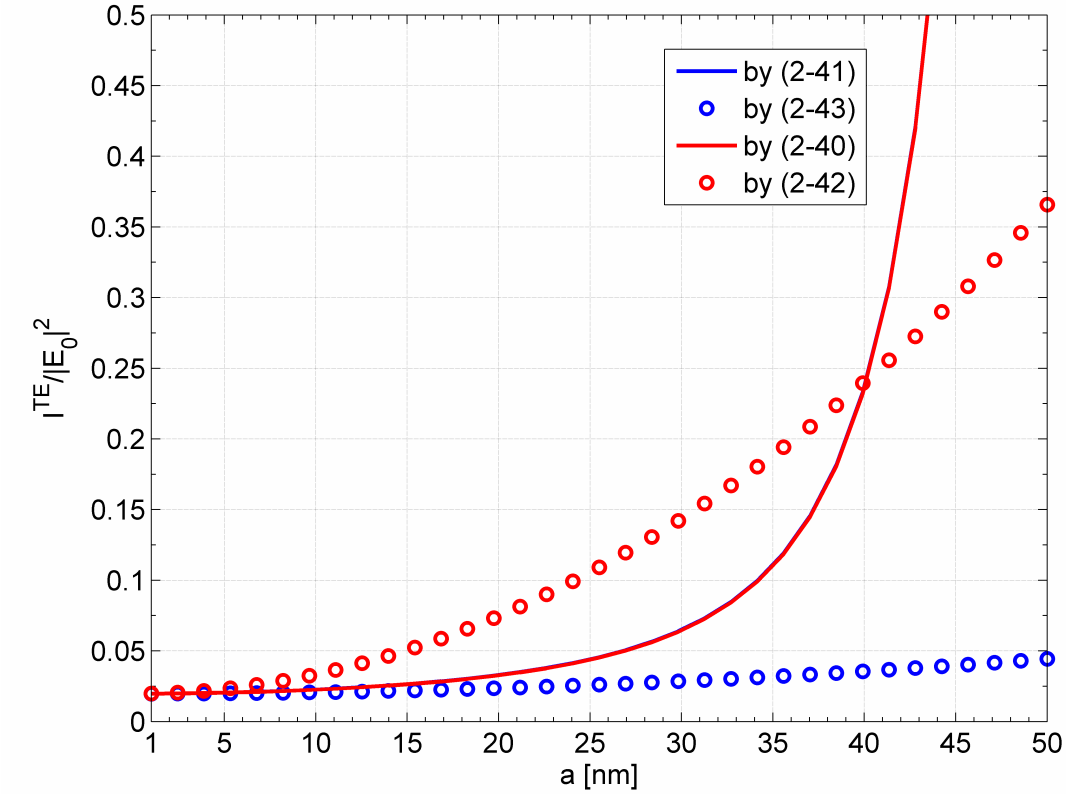

Fig. 2-12: Normalized average internal intensity in GaP nanowire, TE incidence at λ = 488 nm. Lossless expressions (blue) evaluated with $\varepsilon'' = 0$, lossy (red) with $\varepsilon'' = 0.0003$.

2.6 Summary

We examined scattering from infinite cylindrical GaP nanowires. Asymptotic forms were developed for both field expressions and average internal intensities in the limit of small radii. The ratio of orthogonally polarized intensities was found to be in excess of unity, indicating the presence of the dipolar Raman scattering pattern or ‘antenna effect’ as explained in [4].

Chapter 3

Arrays of Nanowires

3.1 Motivation

Antenna arrays at conventional frequencies are often used to increase gain and shape patterns. A single antenna from the array is still functional, albeit with reduced performance. For nanostructures, large arrays are often a functional necessity because the size of each individual element is so small compared with the surrounding world. Interaction with single nanowires is possible [28], but in general we are interested in the ensemble response for most applications, such as field enhanced spectroscopy, method of harmful agent detection or bandstop IR FSS. It is therefore relevant to model nanowires as a doubly periodic planar array.

3.2 Optical Properties of Metals

As mentioned in Section 1.3, a good model of metals in the infrared (50-400 THz) through visible (400-750 THz) frequencies is the hybrid Lorentz-Drude model [10]. The permittivity obtained from this model for metals is plotted in Fig. 3-1. Both the real and imaginary parts exhibit a roll off with increasing frequency. This indicates a transition from a good conductor to a lossy dielectric. In between, the electromagnetic behavior is similar to that of a loosely coupled plasma whose damped oscillations of charge result in a slow wave. This slow wave leads to a shortening of the effective wavelength

experienced by the nanowire [29], [30]. Therefore, the resonant lengths of nanoantennas are significantly shorter in the near infrared and optical regimes compared with directly scaled conventional antenna elements. The relative conductivity, $\left|\frac{\sigma}{\omega\varepsilon_0}\right|$, given in Fig. 3-2 also shows the same roll off with frequency present in the permittivity. Note that aluminum maintains a higher conductivity than the Noble metals throughout the entire frequency range.

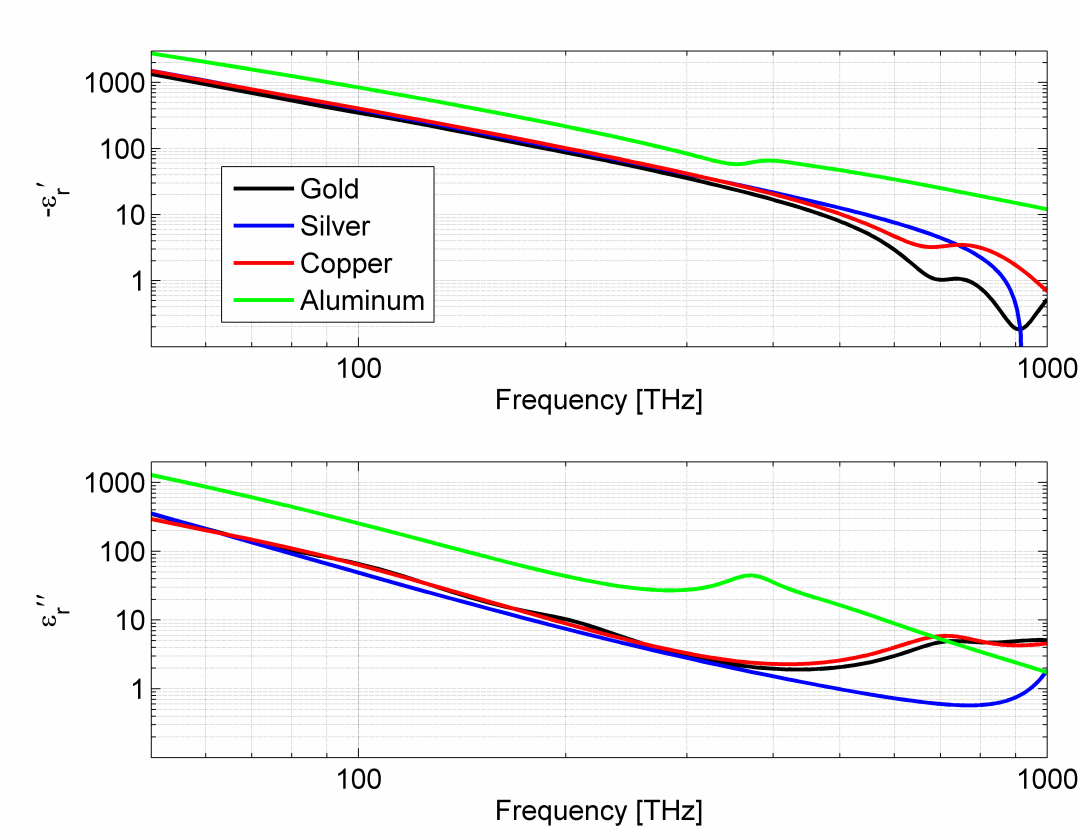

Fig. 3-1: Lorentz-Drude model fitted to metals from 50-1000 THz (6000-300 nm)

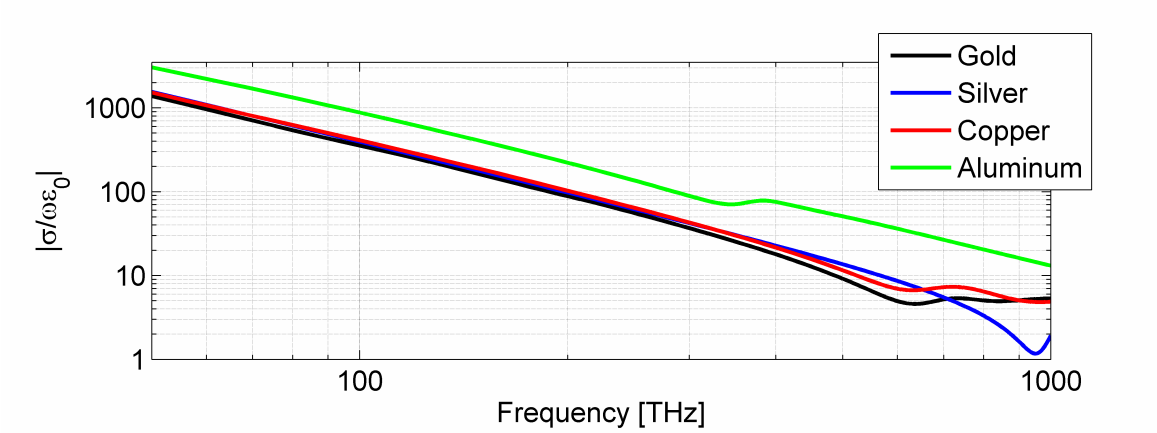

Fig. 3-2: Relative conductivity of metals calculated from Lorentz-Drude permittivity.

3.3 Modeling

A periodic version of the Finite Element Boundary Integral (FEBI) [31] code is used here to effectively model the interaction between elements in an array. This method also has the advantage of directly handling the frequency dependent dielectric profile characterized above. It works by combining both solution techniques of the Finite Element Method (FEM) and the Method of Moments (MoM). Within the unit cell boundary, the fields are solved via FEM. Outside of the boundary, MoM is applied which eliminates the need to discretize the surrounding free space.

Unfortunately, the mesh elements are rectangular 'bricks' which require the cross section to be square whereas most nanowires are circular. This is a minor discrepancy because a strong correlation exists between square and circular conducting elements. To alleviate any concern, an effective radius [32], a_e, may be introduced that approximately

reconciles the two shapes (see Fig. 3-3). For our purposes, we will still refer to the square cross section diameter, *d*.

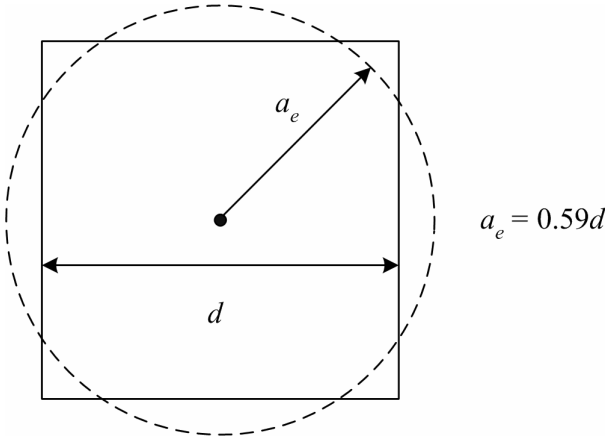

Fig. 3-3: Effective radius for square conductor

The boundary conditions are inherently periodic in the FEBI code. This means the solution obtained is actually for an infinite, planar array of identical elements. Though it is impossible to realize such an array, in practice the interelement coupling in large arrays is nearly identical to that in the infinite case. Even arrays that cover relatively small areas by conventional wisdom will be composed of thousands of nanoelements.

3.4 IR-FSS

In direct analogy to a dipole FSS at RF/microwave frequencies, an array of nanowires can be constructed to reflect radiation in the infrared. The following examples focus on the atmospheric windows of 8-12 μm (37.5-25 THz) and 3-5 μm (100-60 THz) with the goal of producing a stopband roughly at the center of the spectrum.

The unit cell geometry is shown in Fig. 3-4. There are only four degrees of freedom: S_x and S_y determine the interelement spacing; L and d describe the length and diameter of the nanowire. The resonant frequency is directly dependent on L with some small dependence on d. A large interelement spacing reduces coupling between elements, but also introduces some diffraction when (at normal incidence) $S_y > \lambda_{eff}$ for y-polarized waves and $S_x > \lambda_{eff}$ for x-polarized waves. The medium above the structure is assumed to be free space ($\varepsilon_r = 1$) while the medium below is a supportive, electrically large substrate modeled as an infinite half-space. Depending on the wavelength of interest and loss tolerance, this substrate may be glass ($\varepsilon_r \approx 2.25$), polyimide ($\varepsilon_r \approx 3.3$), or silicon ($\varepsilon_r \approx 11.7$).

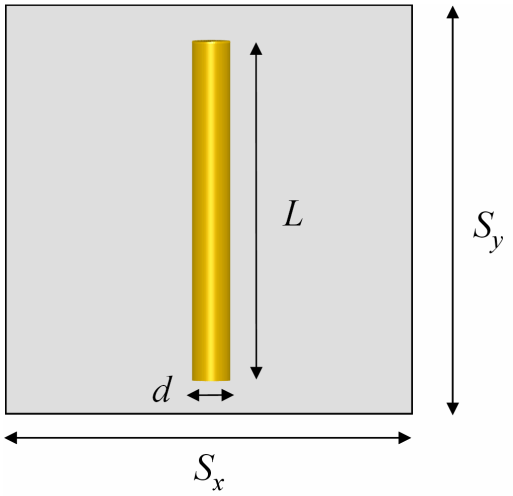

Fig. 3-4: Unit cell geometry for nanowire stopband FSS

The resonant frequency, f_r, corresponding to the stopband location is usually estimated as

$$f_r \approx \frac{c_0}{2L\sqrt{\varepsilon_r^{eff}}} \approx \frac{c_0}{L\sqrt{2(\varepsilon_r + 1)}}. \qquad (3\text{-}1)$$

However, this result does not take into account the effects of reduced conductivity or variation in diameter. Figs. 3-5 and 3-7 show that, for a constant length, increasing the diameter of the wire will: (i) broaden the stopband (increase bandwidth); (ii) shift the stopband to higher frequencies (shorter wavelengths); (iii) increase reflection in the stopband (decrease transmission).

This last result may be due to the penetration of fields and therefore current into the nanowire. The penetration (or skin) depth, δ, in a material depends on both the frequency and complex permittivity.

$$\delta = -\mathrm{Im}\left\{\frac{1}{k}\right\} = -\mathrm{Im}\left\{\frac{1}{\omega\sqrt{\mu\varepsilon}}\right\} = -\frac{c_0}{\omega}\mathrm{Im}\left\{\frac{1}{\sqrt{\varepsilon_r' - j\varepsilon_r''}}\right\} \tag{3-2}$$

The penetration depth defines a rough metric for the attenuation of fields, and therefore current, penetrating into a material. The field strength attenuates to e^{-1} or about 37% of its initial value in the case of a wave incident on an infinite planar surface. For a constant permittivity, the penetration depth decreases with increasing frequency. This leads to a 'skin effect' in metals at high RF and millimeter wave frequencies when δ is so small the majority of current is concentrated within a very thin layer near the metal surface. In this case perturbations in conducting wire diameter have little effect on the current flow because little current occupies the inner cross sectional area of the wire. Recall that Figs. 3-1 and 3-2 show the permittivity and conductivity of metals are far from constant at infrared and optical frequencies. The roll off is fast enough that even for very high values of ω the penetration depth remains finite and actually increases into the optical. Therefore the current flow is strongly dependent on the diameter of the nanowire.

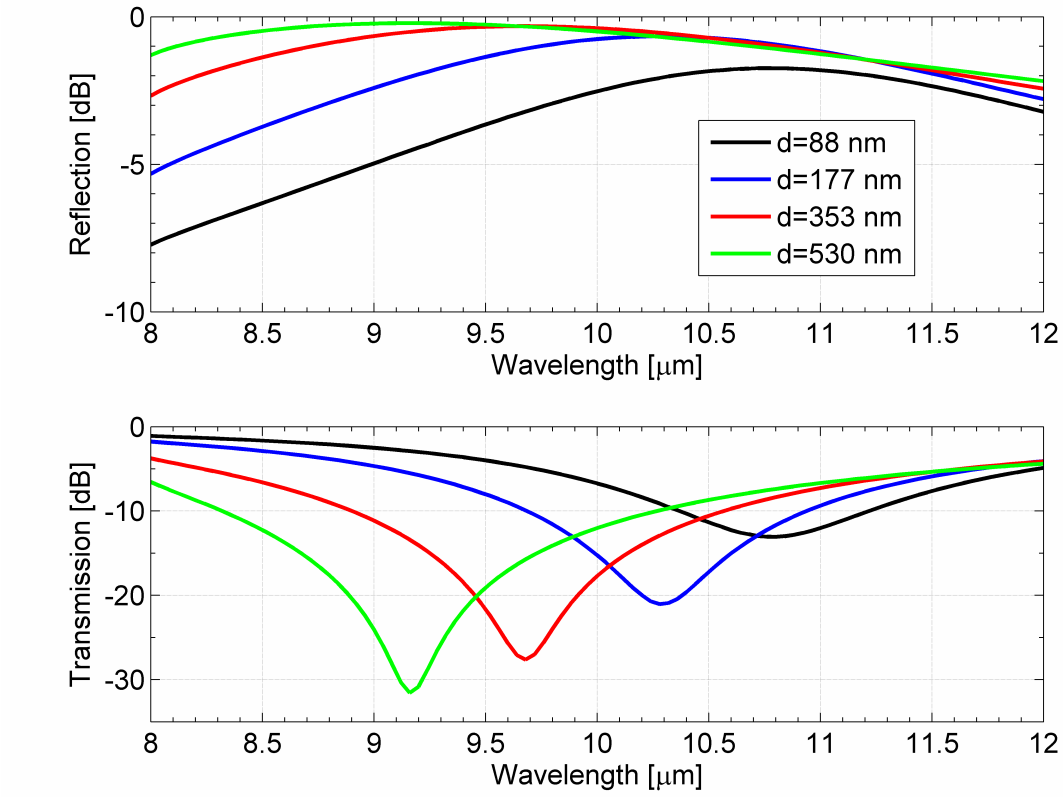

Fig. 3-5: Spectrum for gold nanowire array with variation in d. L =4.063 μm, S_x =3.53 μm, S_y = 5.3 μm, on glass (ε_r = 2.25).

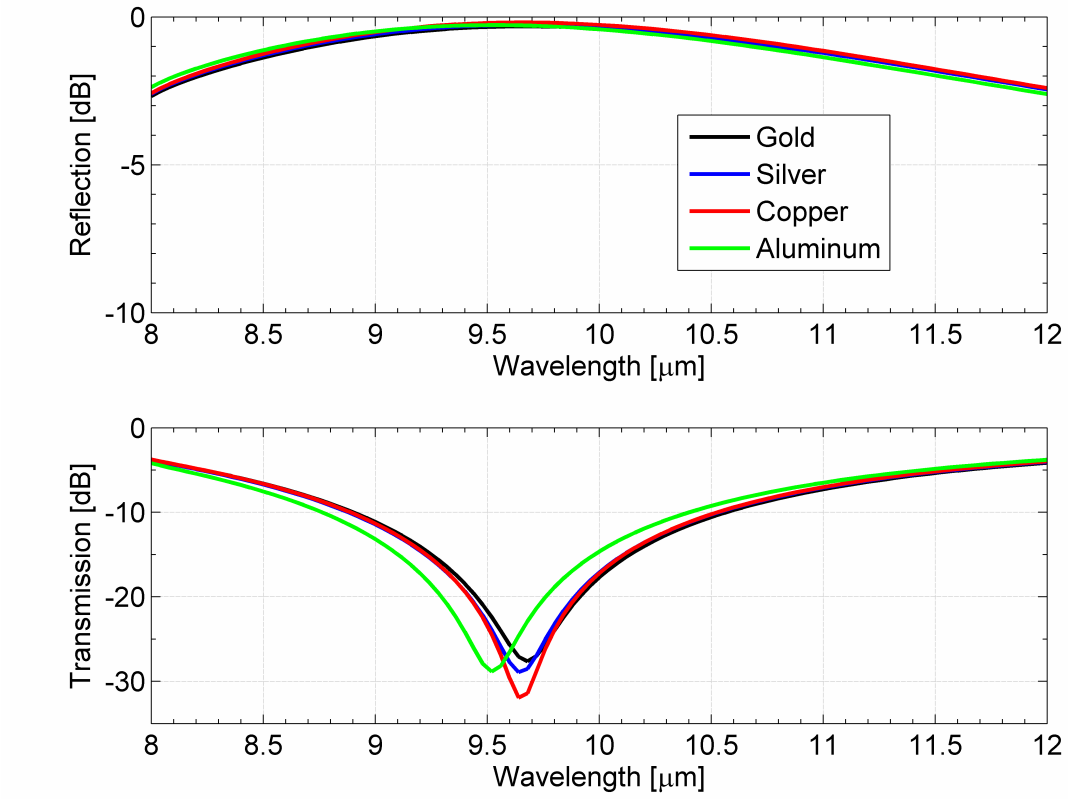

Fig. 3-6: Spectrum for nanowire array with variation in material. L = 4.063 μm, S_x =3.53 μm, S_y = 5.3 μm, d = 353 nm, on glass (ε_r = 2.25).

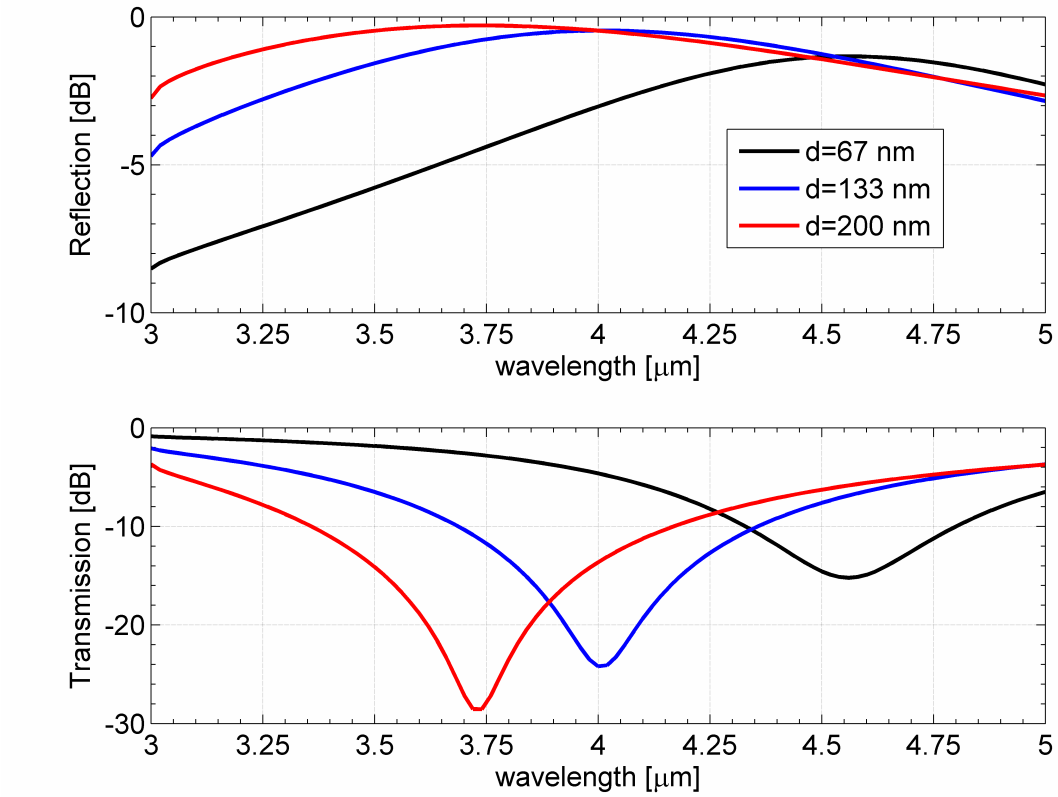

Fig. 3-7: Spectrum for gold nanowire array with variation in d. L = 1.47 μm, S_x = 1.33 μm, S_y = 2.0 μm on glass (ε_r = 2.25).

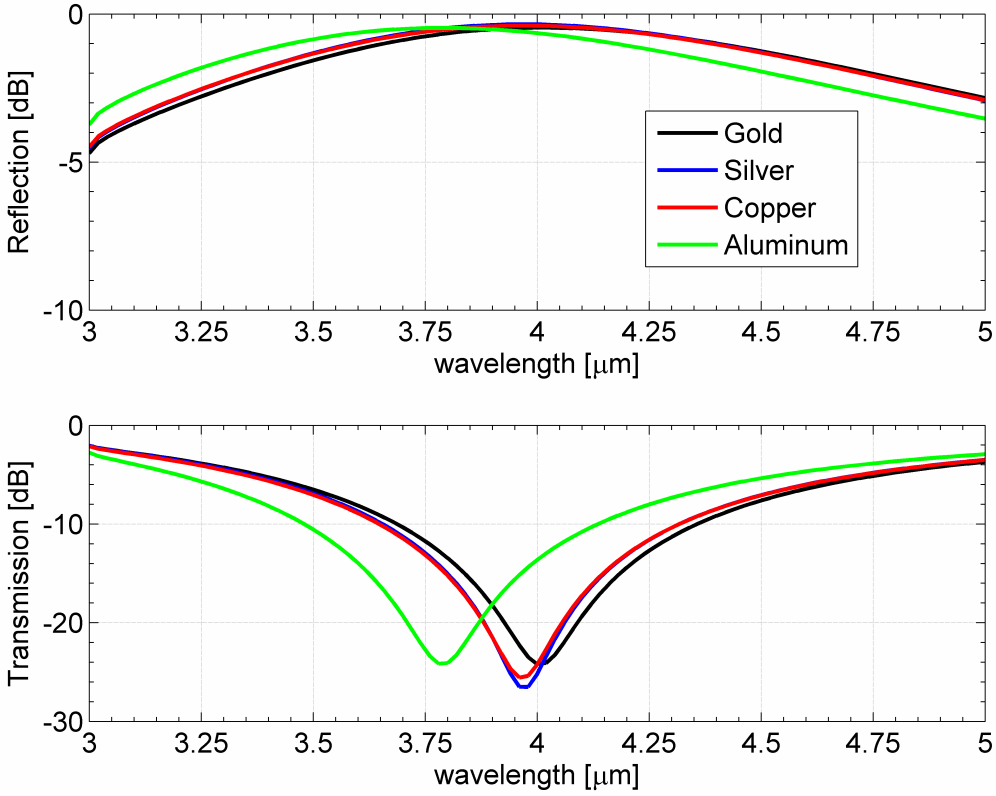

Fig. 3-8: Spectrum for nanowire array with variation in material. L = 1.47 μm, S_x = 1.33 μm, S_y = 2.0 μm, d = 133 nm, on glass (ε_r = 2.25).

Table 3-1: Penetration depth of bulk metals calculated by (3-2)

λ_0 [μm]	f [THz]	δ_{Au} [nm]	δ_{Ag} [nm]	δ_{Al} [nm]	δ_{Cu} [nm]
10	30	26.8	25.2	19.3	24.8
5	60	25.8	24.3	17.3	24.4
3	100	25.5	24.1	16.3	23.7
0.5	600	42.2	28.9	13.5	34.1

Table 3-1 confirms that the smaller diameter nanowires are on the order of δ. Therefore, less induced current flows along the nanowire and, subsequently, the thinner wires exhibit less reflection (and more transmission) in the stopband. The differences between skin depths of different materials at identical frequencies are marginal in the IR with the exception of aluminum. Figs. 3-6 and 3-8 confirm that in the IR, aluminum is the only metal to display any appreciable difference in its transmission/reflection spectrum.

3.5 Field Enhanced Substrate

The signal strength in certain spectroscopic techniques, such as SERS, is dependent upon the local electric field. This local electric field can reach very high values around corners, edges and gaps in plasmonic materials such as metals at optical/IR frequencies. Exploiting the FSS design from above, we can introduce a gap of length, g, in the wire center as in Fig. 3-9. This is similar to the delta feed gap in a conventional RF/microwave dipole but without an impedance matched transmission line. It should be noted that in this configuration the nanowire behaves very poorly as an *optical nanoantenna*, which is the subject of Chapter 4.

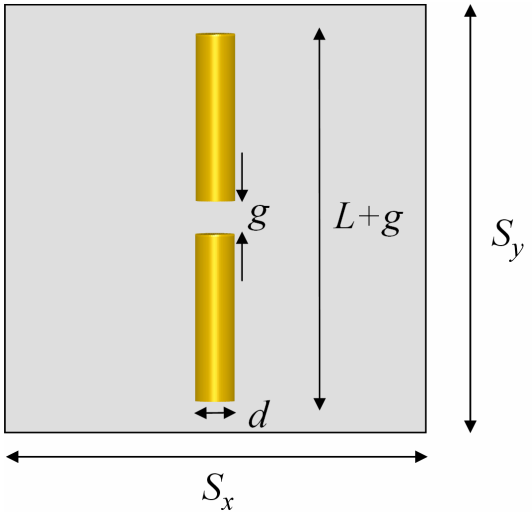

Fig. 3-9: Unit cell geometry of field enhanced substrate

Similar to the IR-FSS studies above, we are interested in determining the parameters (gap size, diameter, material choice) that bring about the best performance. In this case, the performance is measured by the maximum near field value within the gap region. Fig. 3-10 shows the direct correlation between the reflectance maxima and the maximum field enhancement. At the reflection resonance the current is maximized along the nanowire which also maximizes the electric field in the gap. The field enhancement is also heavily dependent on the gap size.

In Fig. 3-11 (g = 5 nm) the field reaches a maximum value of ~ $60E_0$ and is very uniform within the narrow gap. For a larger (g = 20nm) gap, shown in Fig. 3-12, the field is weaker and less uniform. Silver and copper nanowires have both higher reflectance and field enhancement (see Fig. 3-13) than gold due to their slightly better conductivity in this range. The peaks are also shifted to shorter wavelengths. Even though thinner nanowires exhibit less reflectance, Fig. 3-14 shows that the gap field is actually higher. This occurs because the fields are concentrated over a smaller cross sectional area.

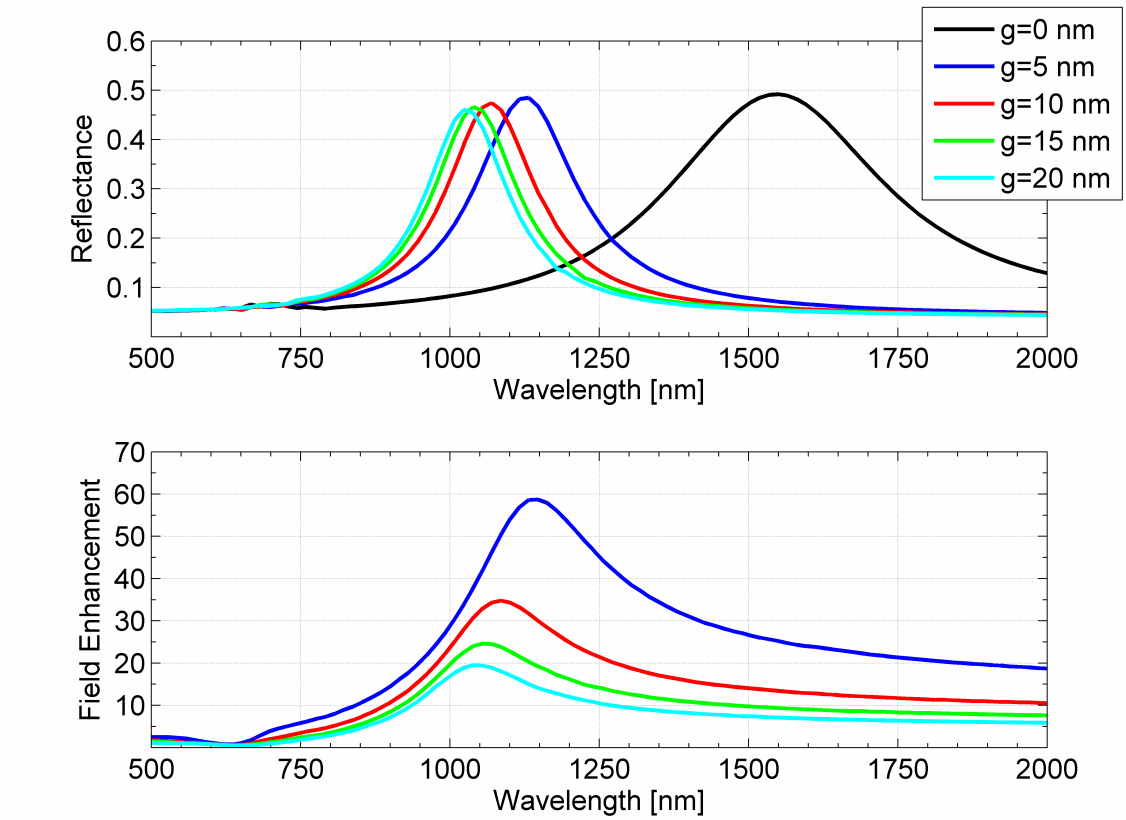

Fig. 3-10: Reflectance and field enhancement for gold nanowires with variation in gap distance. L = 220 nm, S_x = 200 nm, S_y = 300 nm, d = 20 nm, on glass (ε_r = 2.25).

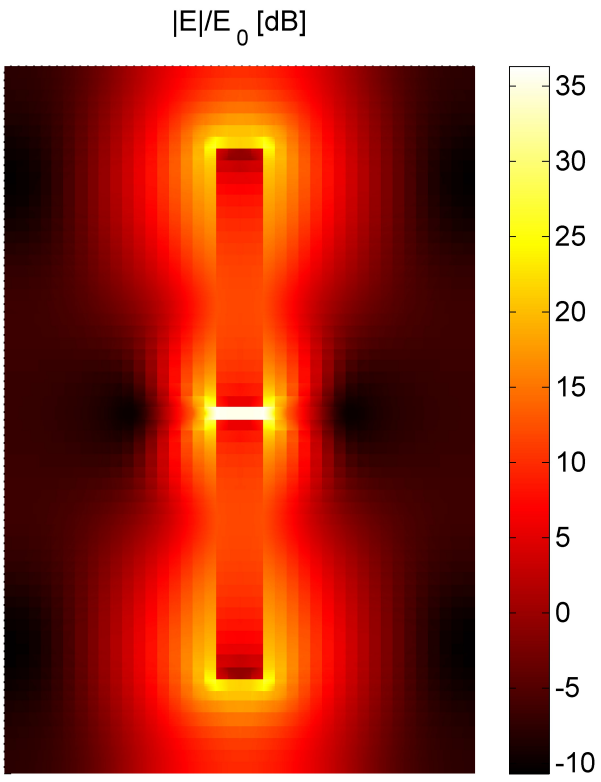

Fig. 3-11: Normalized electric field magnitude in dB for gold nanowire array at resonance ($\lambda_0 = 1132$ nm). $L = 220$ nm, $S_x = 200$ nm, $S_y = 300$ nm, $d = 20$ nm, $g = 5$ nm, on glass ($\varepsilon_r = 2.25$).

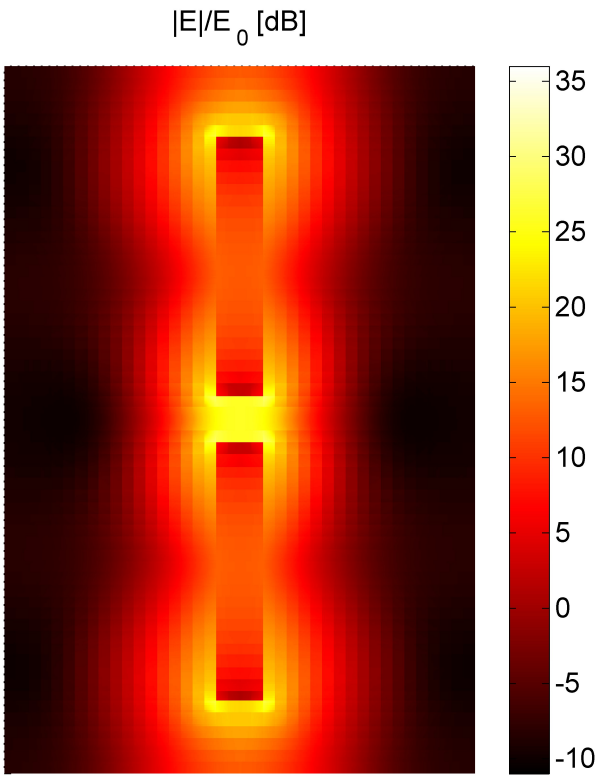

Fig. 3-12: Normalized electric field magnitude in dB for gold nanowire array at resonance ($\lambda_0 = 1039$ nm). $L = 220$ nm, $S_x = 200$ nm, $S_y = 300$ nm, $d = 20$ nm, $g = 20$ nm, on glass ($\varepsilon_r = 2.25$).

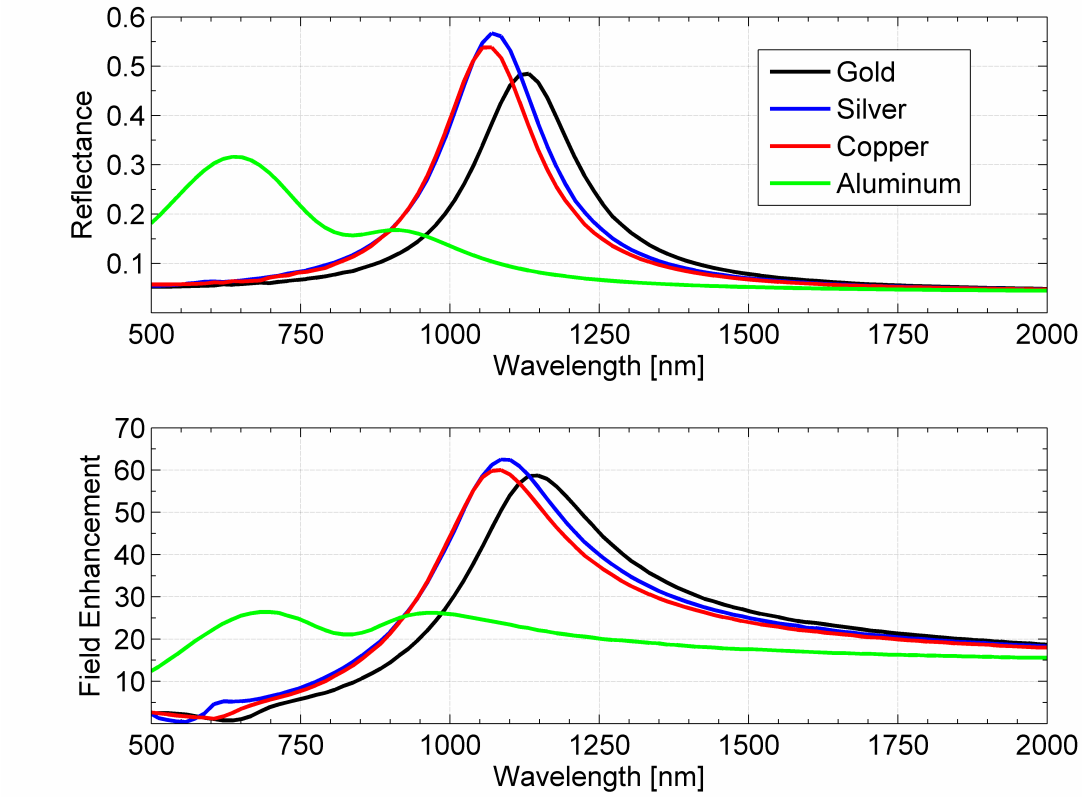

Fig. 3-13: Reflectance and field enhancement for metallic nanowires with variation in nanowire material. L = 220 nm, S_x = 200 nm, S_y = 300 nm, d = 20 nm, g = 5 nm on glass (ε_r = 2.25).

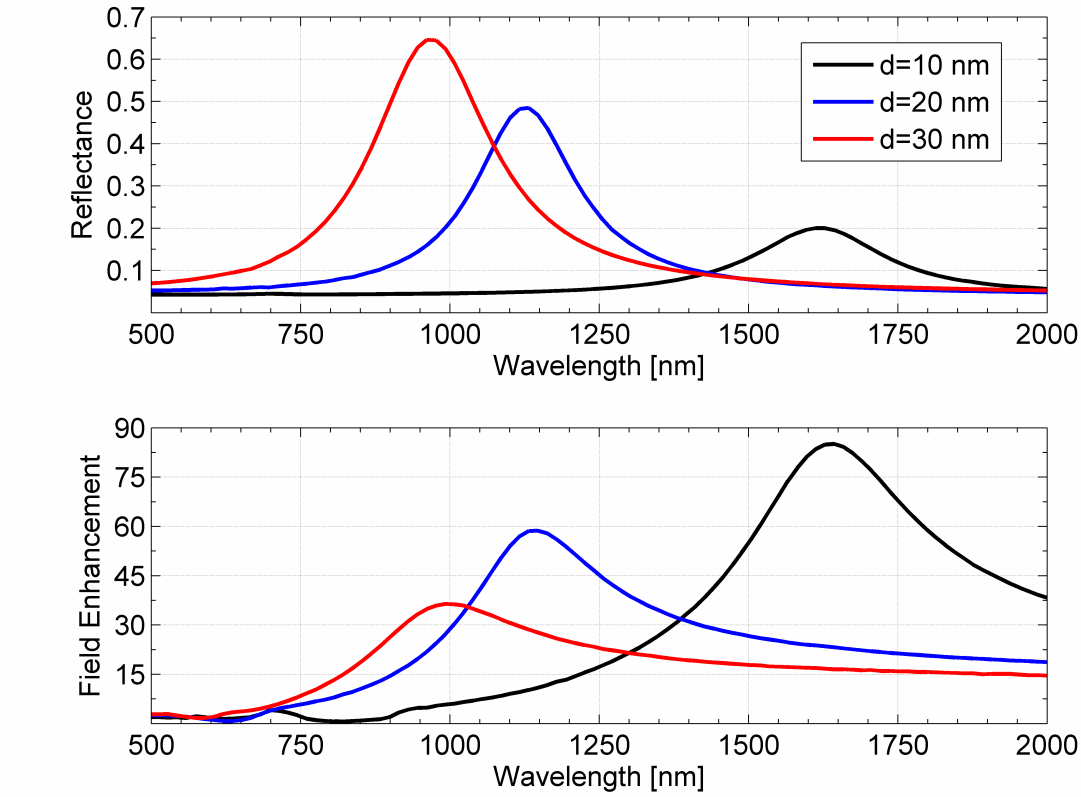

Fig. 3-14: Reflectance and field enhancement for gold nanowires with variation in nanowire diameter, d. L = 220 nm, S_x = 200 nm, S_y = 300 nm, g = 5 nm on glass (ε_r = 2.25).

3.6 Summary

Large arrays of nanowires may be accurately modeled with a periodic FEBI code. This model includes the full dispersive character of metals. Even though metals have reduced conductivity at optical and infrared frequencies, it is still sufficiently high to support current for relevant applications.

Nanowire arrays are effective as IR FSSs. Deep ($|S_{21}| < -20$ dB) stopbands may be produced within both mid-IR windows. The resonant frequency is affected by the type of metal and nanowire diameter as well as the length. This is likely due to the amount of current that the nanowire can support at a given frequency. By placing a short "delta feed" type gap in the wire center, high near fields are produced at the reflection resonance. These fields depend on the material type and nanowire geometry.

Chapter 4

Nanowires as Optical Antennas

4.1 Motivation

At traditional wavelengths, antennas are well known as a bridge between energy radiated in free space and energy contained in the circuit environment. One may imagine that with nanocircuit elements [1], nanoantennas may form the basis for an entirely new approach to optical systems [33],[34]. Optical Yagi-Uda arrays for the directed transmission of light are just one example of how conventional RF concepts may be applied to optics [35].

The previous chapters have examined nanowires as simple scatterers. To make the transition to nanoantennas, we must characterize these nanoelements in terms of their ability to efficiently receive and transmit radiation. These characteristics are fundamental to determining how effectively a nanoantenna may couple light in an optical system.

4.2 Antenna Parameters

The *input impedance*, Z_{in}, of an antenna is defined as the ratio of voltage to current referenced at the pair of input terminals that define the feed in the absence of any load [32]. It is often decomposed into real and imaginary parts

$$Z_{in} = \frac{V_{in}}{I_{in}} = R_{in} + jX_{in} . \tag{4-1}$$

One method of measuring the impedance is to feed the antenna with a constant voltage source and determine the induced current flowing into the antenna. The integral form of Ampere's Law may be invoked to find the total current (both displacement and conduction) from the magnetic field

$$\oint \mathbf{H} \cdot d\mathbf{l} = I_{total} . \tag{4-2}$$

With the accurate evaluation of input impedance, the antenna may be abstracted away into an equivalent Thévenin circuit model. This allows one to match a source or tune the antenna resonances using conventional circuit techniques.

The *radiation efficiency*, e_r, of an antenna is a measure of the power lost by the antenna when radiating into free space. It can be expressed as the ratio of power radiated by the antenna to the input power, that is

$$e_r = \frac{P_{rad}}{P_{in}} . \tag{4-3}$$

The radiated power is obtained by integrating the average power flow (via the time-average Poynting vector, $\mathbf{S_{av}}$) through a closed surface enclosing the antenna,

$$P_{rad} = \oiint \mathbf{S_{av}} \cdot d\mathbf{s} , \tag{4-4}$$

while the real input power is obtained from the circuital relation

$$P_{in} = \frac{1}{2} \mathrm{Re}\left\{ VI^* \right\} . \tag{4-5}$$

In good conductors the radiation efficiency is usually near unity, but, as shown previously, real metals exhibit varying amounts of loss and dispersion at optical frequencies. We therefore expect to find low values of efficiency, at least when compared

with conventional RF antennas. The efficiency can also be written in terms of the *radiation resistance*, R_r, and the *ohmic* or *loss resistance*, R_{loss} (4-6). The power accepted by the antenna is either dissipated in the loss resistance as heat or in the radiation resistance as an electromagnetic wave propagating into free space. We also assume that the input resistance, R_{in} is equivalent to R_r and R_{loss} in series.

$$e_r = \frac{R_r}{R_r + R_{loss}} \tag{4-6}$$

Another pair of parameters is the *directivity* and *gain* of an antenna. The directivity relates the radiation pattern of the antenna to that of an isotropic source. Written in terms of average power flow and radiated power,

$$D = \frac{4\pi r^2 S_{rad}}{P_{rad}}, \tag{4-7}$$

where r is the radial distance from the antenna. This may also be written in terms of the far-field power pattern, $F(\theta, \varphi)$,

$$D = 4\pi \frac{F(\theta,\varphi)}{\int_0^{2\pi}\int_0^{\pi} F(\theta,\varphi)\sin\theta d\theta d\varphi} \tag{4-8}$$

The *gain* (4-9) is related to the directivity by the radiation efficiency and therefore includes energy lost from within the antenna. Both of these parameters have their meaning strictly in the far field [32].

$$G = e_r D \tag{4-9}$$

4.3 Problem Geometry

COMSOL Multiphysics®, a general finite element code, was used in axisymmetric, transverse magnetic (TM) mode to simulate a single, transmitting nanodipole in free space. This mode reduces the full three dimensional problem to a two dimensional one by assuming constant field values with respect to the azimuthal angle φ. Furthermore, only TM field components are accounted for, that is E_ρ, E_z, and H_φ. This drastically reduces the computational complexity of the problem and allows us to use a very fine finite element mesh. The dipole (see Fig. 4-1) consists of two metallic cylinders of radius a separated by a feed gap (similar to section 3.5) of distance g, centered in the standard cylindrical coordinate system along the z axis. The total length of both the cylinders and feed gap is L.

The entire simulation domain is enclosed in a sphere of free space (actually a semicircle in the two dimensional, axisymmetric mode) with a scattering boundary condition to eliminate reflections from propagating waves in the far field. This boundary extents at least one free space wavelength from the antenna at the lowest simulated frequency (100 THz).

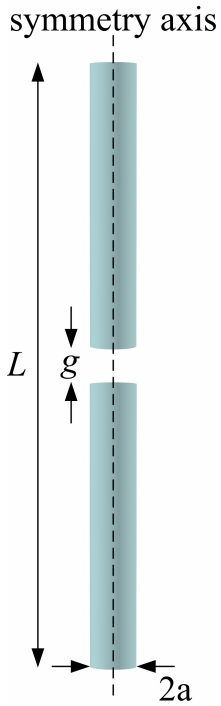

Fig. 4-1: Nanodipole geometry with symmetry axis.

4.3.1 Meshing Requirements

The standard meshing criterion calls for discretization at least every $\lambda_{eff}/10$. This, however, assumes minimal loss and field variation. Around feed regions and sharp discontinuities this requirement may need to be reduced significantly. In addition, the skin depth of the material, which for metals is many orders smaller than the effective wavelength, must also be resolved by a few mesh elements. Fortunately, COMSOL Multiphysics® allows one to customize an inhomogeneous mesh. Therefore we use a coarse mesh in free space, a fine mesh inside the metal and at the metal/air interface, and

an even finer mesh around the feed region. Typical mesh dimensions are summarized in Table 4-1.

Table 4-1: Typical mesh dimensions used in COMSOL for f_{max}= 700 THz (λ_0= 430 nm) in terms of physical and electrical length.

	Free Space	Metal Volume	Feed Gap
Max mesh size [nm]	40	1	0.2
Max mesh size [λ_0]	0.093	$2.4\text{x}10^{-3}$	$4.8\text{x}10^{-4}$
Max mesh size [λ_{Ag}]	0.013	$3.2\text{x}10^{-4}$	$6.4\text{x}10^{-5}$
Max mesh size [δ_{Ag}]	1.24	0.031	$6.2\text{x}10^{-3}$

4.3.2 Feed Method

Ideally, the feed configuration in an antenna simulation should correlate directly to the physical feed when the antenna is realized in a system. Physical feeds are still the source of much speculation for optical nanoantennas because they are, by nature, highly subwavelength in size. Subwavelength feeds are no obstacle at conventional RF wavelengths (meters to millimeters), but their realization becomes more and more complicated at optical/IR wavelengths (microns to nanometers). Some novel methods that avoid an explicit subwavelength feed are being researched [36], but for the purposes of this study, a conventional delta gap feed is assumed. Though the exact values determined from a delta gap feed may differ from a more physical source, the predictions should at least agree qualitatively and provide a good estimation of optical nanoantenna performance.

The delta gap feed consists of an impressed electric field between the center circumferences of the two cylinders. This is illustrated in Fig. 4-2. The electric field is

normalized by the gap distance to produce a voltage of unity. The current and therefore the input impedance are then measured by application of (4-2).

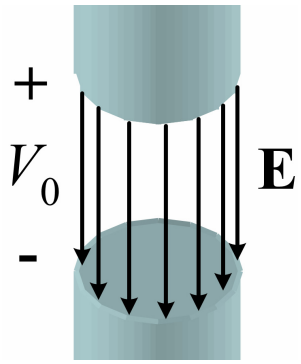

Fig. 4-2: Delta gap feed model.

4.4 Results

4.4.1 Input Impedance

The input impedance was obtained via application of *Ampere's Law* (4-2) with a contour around the corresponding nanowire radius, a, at the gap center, $z = 0$. This choice effectively measures the total current flowing into the antenna by sampling the magnetic field at $r = a$, $z = 0$, which is away from the actual nanowire edge. This avoids the large field discontinuities present at the edge that give nonphysical results for Z_{in}.

The following impedance curves share several key features with conventional, thin-wire RF antennas: (i) below the first resonance, the reactance is very capacitive (negative) corresponding to a short dipole; (ii) there is a low impedance resonance (characterized by the first reactance zero) corresponding to a half-wave dipole; (iii) there is a high impedance resonance (characterized by the second reactance zero)

corresponding to a full-wave dipole. This behavior repeats for higher orders with increasing frequency.

In contrast to conventional antennas, the impedance resonances do not occur at half-integer multiples of the exciting free space wavelength. They instead correspond to an effective wavelength which scales based on the nanoantenna geometry and frequency dependent material parameters [29]. The spacing between resonances tend to decrease in the optical (~400-700 THz) as a consequence because this scaling changes as a function of frequency.

There is an obvious frequency shift in the impedance resonances with variation in the nanoantenna length as in Fig. 4-3. Due to the optical wavelength scaling, shortening a nanoantenna by one half of its original, physical length does *not* double its resonant frequency. An L = 200 nm, a = 10 nm, g = 5 nm silver nanodipole resonates at $f \approx$ 300 THz. Shortening the antenna length to L = 100 nm shifts the resonance to $f \approx$ 450 THz. This does correspond to halving the *effective wavelength*, λ_{eff}, but reduces λ_0 to only two-thirds of its original value (see Table 4-2).

Table 4-2: Effective wavelength for silver nanoantennas (a=10 nm, g=5 nm) extracted from impedance data for the $L \approx \lambda_{eff}/2$ resonance.

f_r [THz]	L [nm]	λ_0 [nm]	λ_{eff} [nm]
187.65	400	1599	800
300	200	1000	400
450	100	667	200

Changing the nanoantenna radius also has a profound impact on the impedance curves (shown in Fig. 4-4). Larger radius nanowires generally have less resonant peaks and these peaks are also of a lesser magnitude for both the input resistance and input

reactance. This is in contrast to thin-wire RF antennas where only the input reactance is affected by the wire radius [32]. The location of the resonances also shifts to higher frequencies with increased nanowire radius. These changes are expected because a is on the order of δ and therefore small changes in a will greatly affect the induced current along the nanoantenna.

Changing the nanoantenna material from silver to similar noble metals, such as copper and gold, only has a small impact on the input impedance. This is plotted in Fig. 4-5. Due to the lower conductivity of gold and copper beyond 500 THz, the second set of resonances (corresponding to $L \approx 3\lambda_{eff}/2$ and $L \approx 2\lambda_{eff}$) are damped compared with silver and X_{in} never reaches zero. Aluminum has a very different dispersion profile from silver, gold and copper. The conductivity remains relatively large even at higher frequencies and, as a consequence, an aluminum nanoantenna (L = 200 nm, a = 10 nm) first resonates at $f \approx$ 450 THz. This is much higher in frequency than other comparably sized nanoantennas made of noble metals.

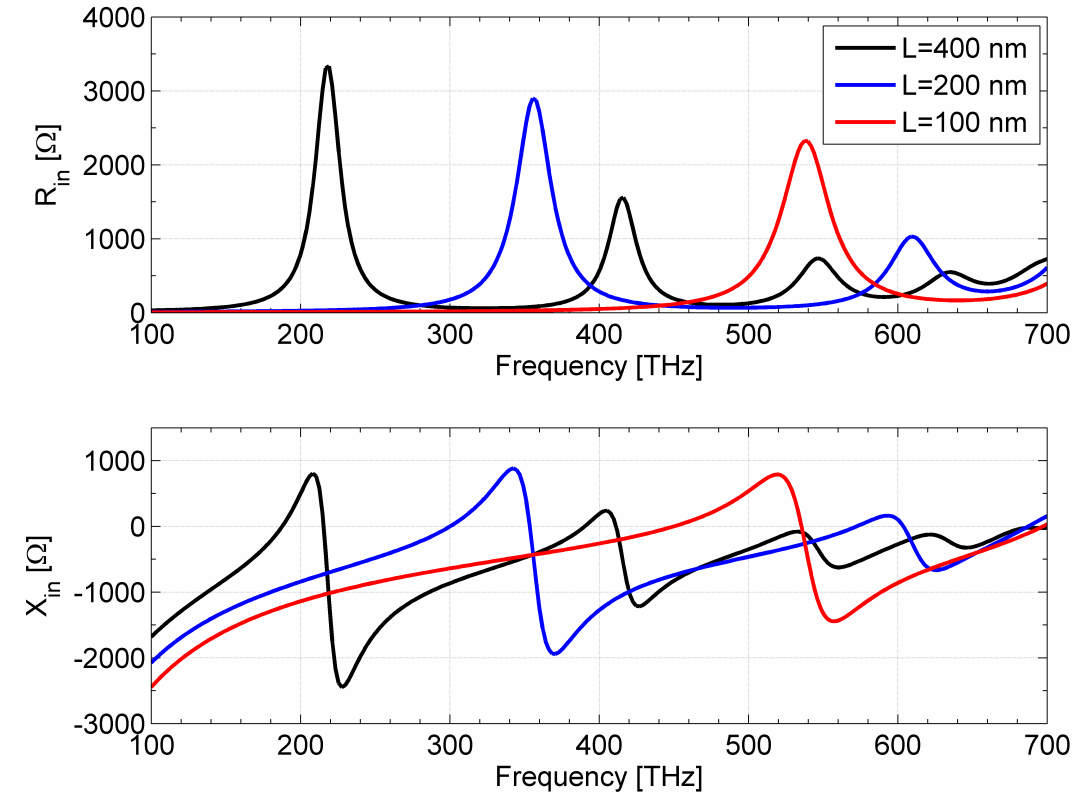

Fig. 4-3: Input impedance for silver nanoantenna, a=10 nm, g=5 nm with variation in L.

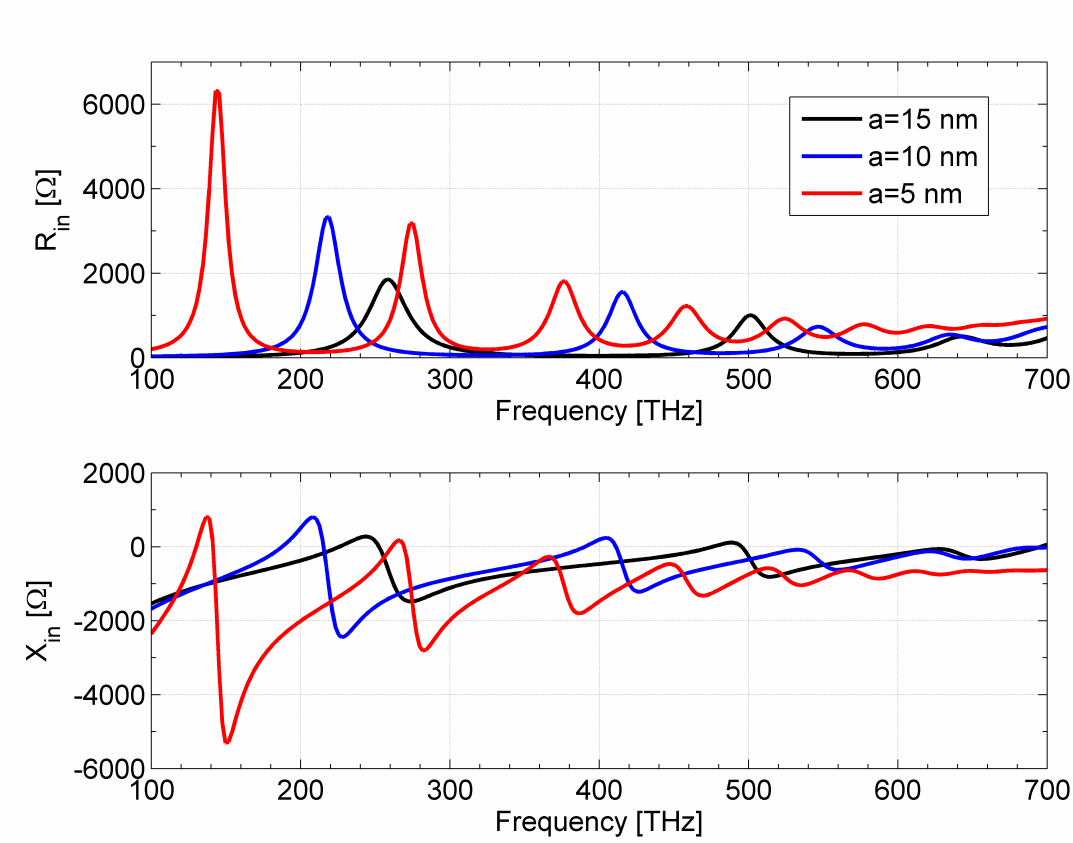

Fig. 4-4: Input impedance for silver nanoantenna, L=400 nm, g=5 nm with variation in a.

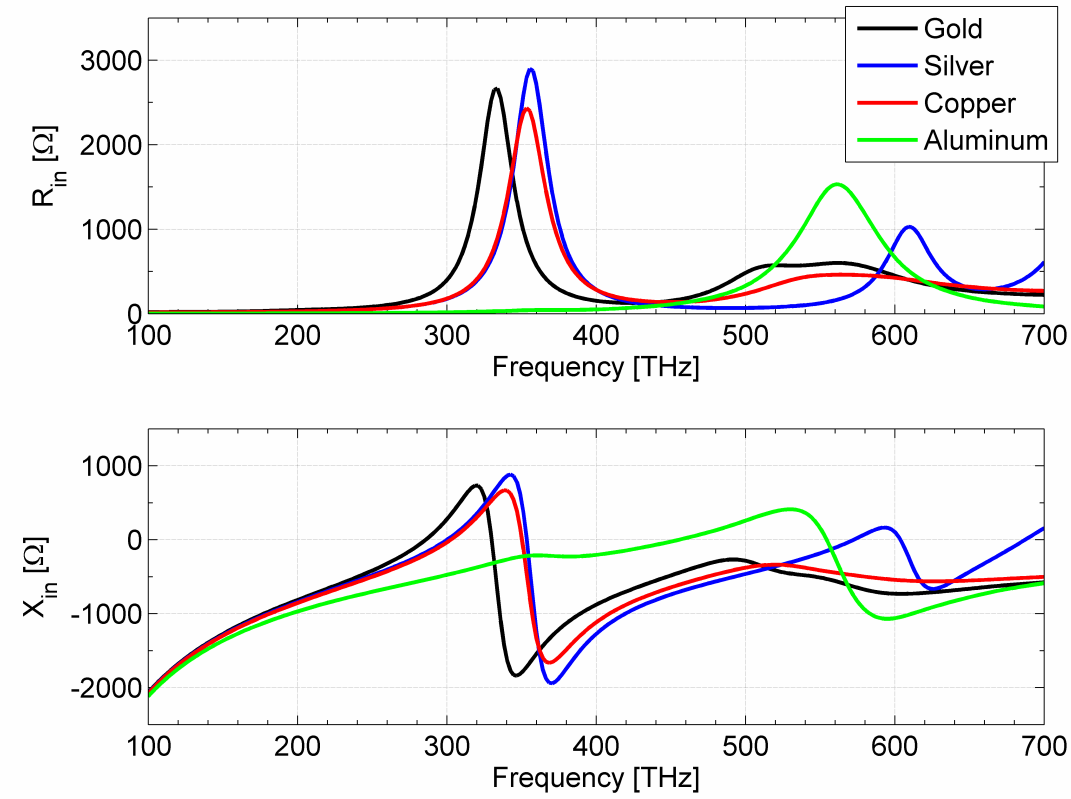

Fig. 4-5: Input impedance for nanoantenna, L=200 nm, a=10 nm composed of different metals.

4.4.2 Radiation Efficiency

The radiation efficiency of an antenna is dependent on both the bulk material loss and also the current distribution along the antenna. Since the conductivity of metals rolls off at optical frequencies, one would expect nanoantennas resonant at higher frequencies to be less efficient. This is, in general, true but not the dominant mechanism. The nanoantenna diameter also plays an important role.

In Table 4-3 a resonant L = 100 nm silver dipole is about 4% less efficient than an L = 200 nm dipole with constant radius. The difference in efficiency is even smaller between L = 400 nm and L = 200 nm dipoles (less than 1%). Changing the radius has a much greater effect on the radiation efficiency. Even though a thicker dipole resonates at a higher (and therefore more lossy) frequency, the efficiency actually increases with radius. Efficient optical nanodipoles must have a smaller aspect ratio than their RF/PEC equivalents. This is consistent with the surface impedance approach in [6].

Table 4-3: Radiation efficiency corresponding to the first ($L \approx \lambda_{eff}/2$) resonance for silver nanoantennas.

f_r [THz]	L [nm]	a [nm]	Z_{in} [Ω]	e_r [%]	R_r [Ω]
450	100	10	$115.16 + j0.05$	16.67	19.2
300	200	10	$175.57 - j1.75$	20.3	35.64
130.14	400	5	$1272 + j0.75$	4.52	57.5
187.65	400	10	$334.76 - j1.1$	20.39	68.26
224.6	400	15	$310.76 - j0.32$	29.39	91.33

Operating near the $L \approx \lambda_{eff}$ resonance changes the current distribution along the antenna. The current flowing into the antenna from the feed is much smaller (it is considered identically zero in some analysis [32]) and, subsequently, the impedance is much higher. The radiation efficiency in this mode, given in Table 4-4, is greater than or

equal to the $L \approx \lambda_{eff}/2$ mode and may also be of interest for matching to high impedance sources or loads.

Table 4-4: Radiation efficiency corresponding to the second ($L \approx \lambda_{eff}$) resonance for silver nanoantennas.

f_r [THz]	L [nm]	a [nm]	Z_{in} [Ω]	e_r [%]	R_r [Ω]
535.45	100	10	$2279 - j0.82$	19	433
353.47	200	10	$2802 + j1.11$	22.82	639.4
141.37	400	5	$5503 + j0.46$	4.97	273.5
215.45	400	10	$3141 - j1.63$	23.11	725.9
253.29	400	15	$1636 - j0.25$	31.33	512.6

As with the input impedance, nanoantennas composed of similar metals have approximately the same radiation efficiency (see Table 4-5). Aluminum nanodipoles, however, have more than 3 times the radiation efficiency as silver nanodipoles. Their first resonance is also in the red (~455 THz or 660 nm) as opposed to the IR. This distinction is clearly important when considering nanoantennas for visible applications.

Table 4-5: Radiation efficiency corresponding to the first ($L \approx \lambda_{eff}/2$) resonance for L = 200 nm, a = 10 nm, g = 5 nm nanoantennas.

f_r [THz]	Material	Z_{in} [Ω]	e_r [%]	R_r [Ω]
300	Silver	$175.57 - j1.75$	20.3	35.64
285.8	Gold	$216.23 - j0.16$	15.17	32.8
302.67	Copper	$196.55 - j0.77$	18.71	36.77
455.17	Aluminum	$122.23 - j1.11$	67.46	82.45

4.4.3 Radiation Pattern

The far field radiation pattern is determined by the current distribution on the antenna. In conventional, thin-wire RF dipoles, the current distribution is very close to sinusoidal. The operating frequency determines the exact shape of this current

distribution and, therefore, the radiation pattern. A short dipole has a different pattern than a half-wave dipole, which has a different pattern than a full-wave dipole and so forth. This behavior at RF assumes that the wavelength of the current distribution is nearly identical to that in free space. Again, the oscillations along optical nanoantennas scale according to the dispersive material parameters and geometry. There is a disparity between the standing current wave and the actual radiated wave.

The radiation pattern at the first two resonances ($L \approx \lambda_{eff}/2$ and $L \approx \lambda_{eff}$) closely follows that of an electrically short dipole (see Fig. 4-6). This makes intuitive sense because the physical antenna length (L = 400 nm) is relatively small with regard to these radiated wavelengths (1604 and 1395 nm, respectively). The third ($L \approx 3\lambda_{eff}/2$) resonance produces sidelobes in the radiation pattern. This is due to the increased complexity in the current distribution along the dipole shown in Fig. 4-7. Also, the antenna length is no longer very short compared with the radiated free space wavelength (769 nm).

Table 4-6 summarizes the maximum directivity and gain computed by (4-8) and (4-9). Again, because of the disparity between the effective and radiated wavelengths, the directivity is approximately between that of a short dipole ($D_0 \approx 1.5$) and a half-wave dipole ($D_0 \approx 1.643$), depending on the resonant frequency and antenna geometry. Due to the reduced efficiency of noble metals at optical frequencies, only the aluminum nanoantenna produced a gain in excess of unity.

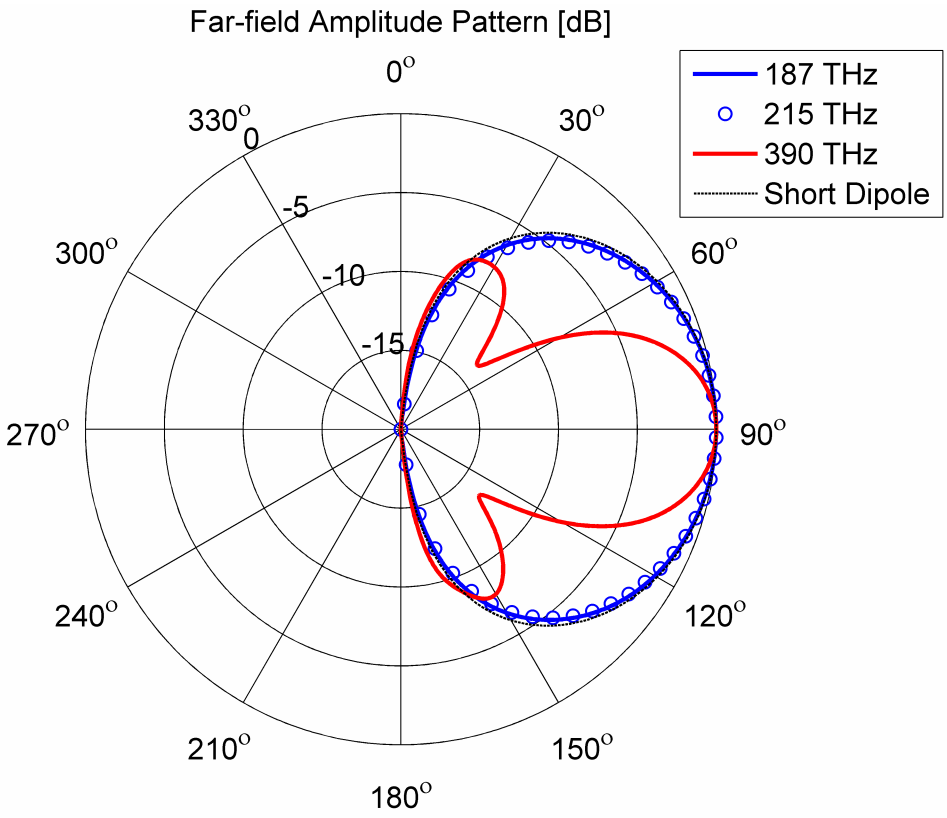

Fig. 4-6: Normalized far-field amplitude pattern of a silver, L = 400 nm, a = 10 nm, g = 5 nm nanoantenna at the first three resonances compared with an ideal short dipole. Pattern is rotationally symmetric about the z axis.

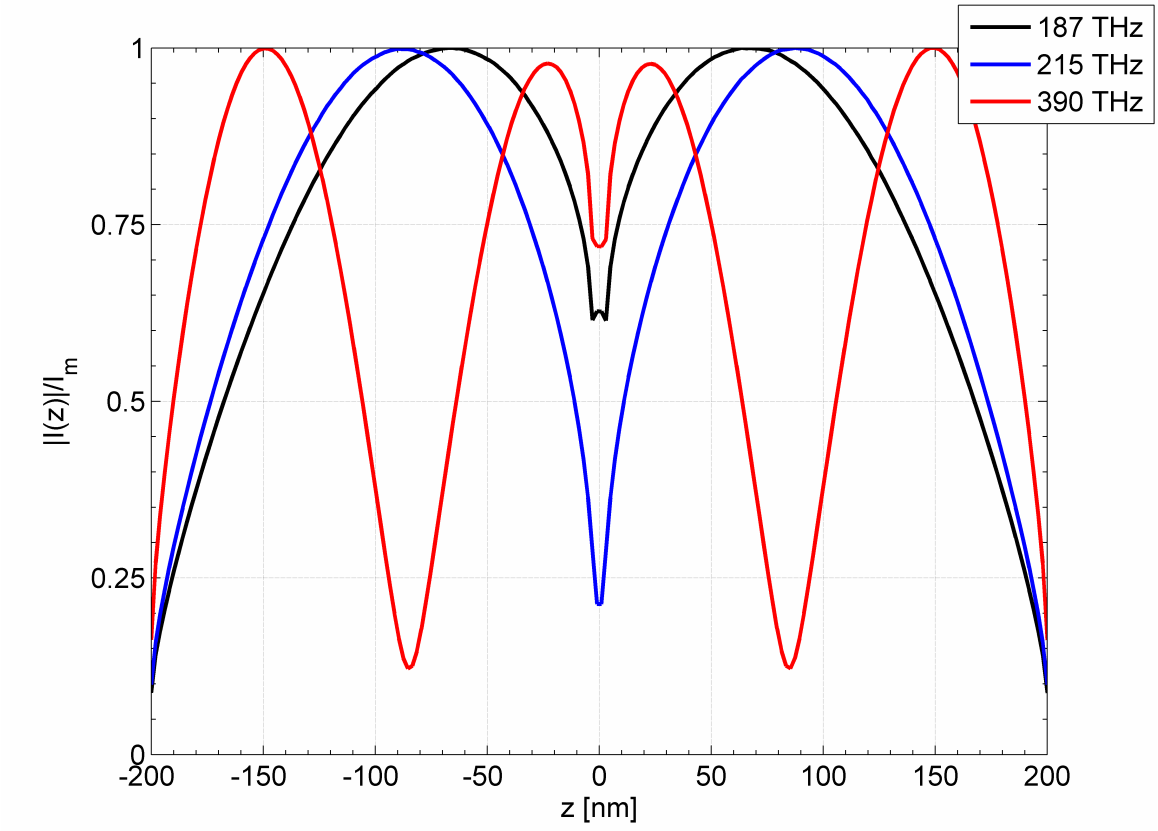

Fig. 4-7: Current distribution along silver, L = 400 nm, a = 10 nm, g = 5 nm nanoantenna at three different frequencies. Each curve is normalized to its respective maximum value.

Table 4-6: Maximum directivity (θ = 90°) and gain for several different nanoantennas at $L \approx \lambda_{eff}/2$ resonance.

f_r [THz]	L [nm]	a [nm]	Material	D_0	G_0
130.14	400	5	Silver	1.52	0.07
187.65	400	10	Silver	1.55	0.32
224.6	400	15	Silver	1.66	0.49
286	200	10	Gold	1.64	0.25
300	200	10	Silver	1.53	0.31
303	200	10	Copper	1.53	0.29
455	200	10	Aluminum	1.67	1.13

4.5 Comparison with Surface Impedance Model

The surface impedance formulation simplifies the boundary problem by reducing the number of unknowns in the simulation. Rather than allow volume current within the material, only surface current is considered. This eliminates the need to discretize the entire material volume as a lossy dielectric. To account for the dispersive and lossy optical properties, the surface current is modulated by a frequency-varying impedance. This surface impedance depends on the antenna geometry and material parameters.

Considering the same cylindrical dipole geometry from above, the total surface impedance is

$$Z_s = R_s + jX_s = \frac{\eta_0}{\sqrt{\varepsilon_{rm}}} \frac{\mathrm{I}_0\left(jk_m a\right)}{\mathrm{I}_1\left(jk_m a\right)} \tag{4-10}$$

where η_0 is the free space impedance, ε_{rm} the relative permittivity of the metal, k_m the propagation constant in the metal, a the cylinder radius and I_0 and I_1 are, respectively, the modified Bessel functions of the first and second kind. A full derivation of this quantity is given in the Appendix. Similar to a standard RLC circuit, the resistance accounts for

energy lost, the reactance accounts for energy stored and both influence the resonant frequency. Notice in Fig. 4-8 the surface reactance for silver becomes capacitive a little beyond 900 THz. This corresponds to the sign change in the permittivity of silver (see Fig. 3-1). The surface impedance was implemented in COMSOL with the identical meshing and feed configuration described in section 4.3.

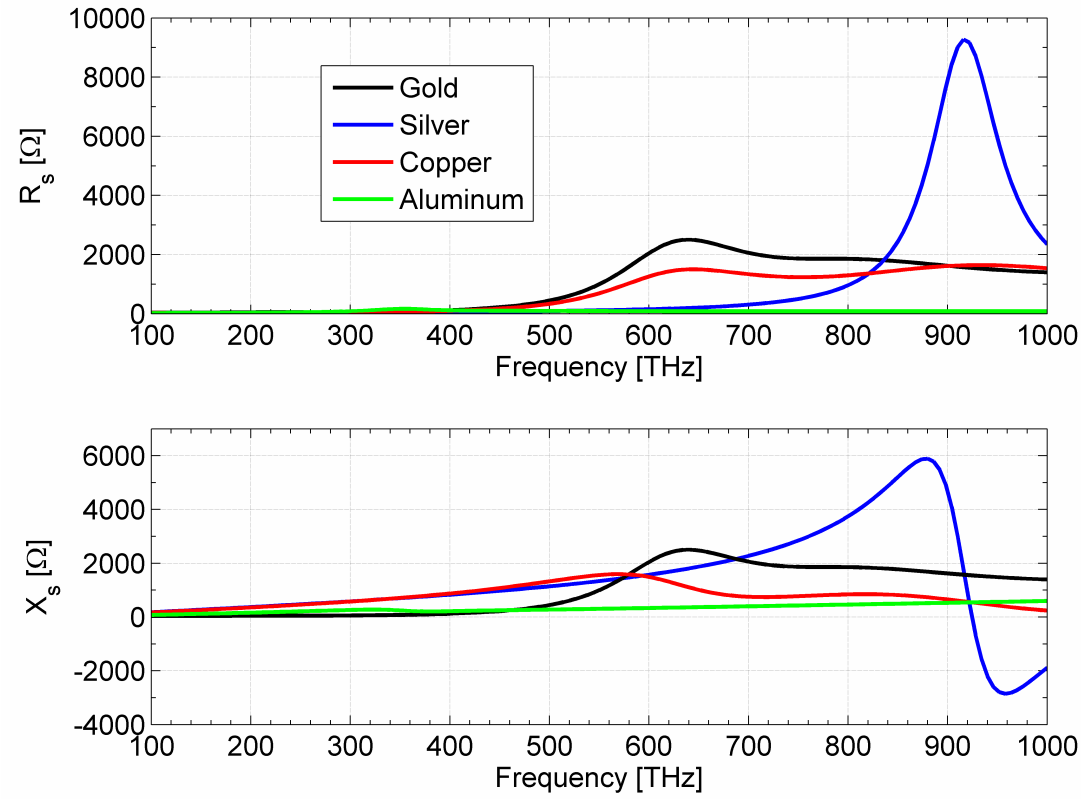

Fig. 4-8: Surface impedance for several a = 5 nm metallic cylinders.

Fig. 4-9 shows a comparison of input impedances calculated by the surface impedance and the full discretization methods. There is excellent agreement in the input resistance for both silver and gold nanodipoles across the 100-700 THz band. The surface impedance method seems to underestimate the capacitance at lower terahertz frequencies

(~100-200 THz). Beyond the first two resonances, the two methods agree better in the calculation of input reactance.

To examine this difference further, let us consider the current distribution along the antenna. The total current is found using Ampere's Law (4-2) at the nanoantenna surface. It is important to remember that only surface current flows when using the surface impedance condition whereas volume current will flow in reality (and also does when discretizing the material volume). (4-2) properly integrates both to give the total current in Amperes. The total current magnitude along the antenna at three different frequencies is given in Fig. 4-10. Both methods calculate similar standing waves away from the feed gap. Near the feed region, the current changes more rapidly using full discretization. This is due to the boundary conditions at the feed; the fields are discontinuous at the source but must be *continuous* across the material boundary. With the surface impedance condition, the fields are *discontinuous* across the material boundary. It also appears that the two different methods match better at the higher frequency (300 THz).

Fig. 4-11 separates the current distribution into real and imaginary parts. Again, agreement is better at 300 THz than otherwise. At 200 THz, the full discretization and surface impedance condition calculate opposite signs for the imaginary part of the current distribution. This explains the difference in the input reactance at 200 THz shown in Fig. 4-9.

A comparison of the far-field patterns is given in Fig. 4-12. The agreement is excellent between the two methods at all three frequencies even though Fig. 4-10 shows a discrepancy in their respective current distributions.

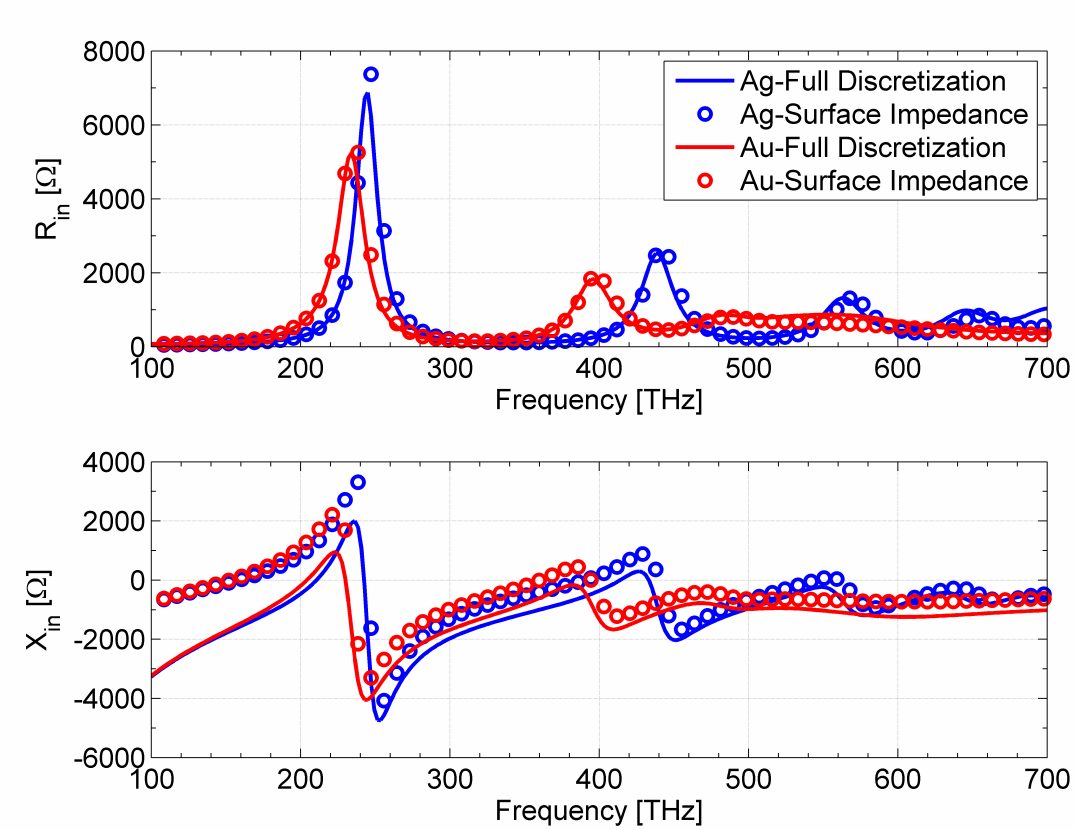

Fig. 4-9: Comparison between input impedances calculated by the full discretization and surface impedance methods for L = 200 nm, a = 5 nm, g = 5 nm, silver (Ag) and gold (Au) nanodipoles.

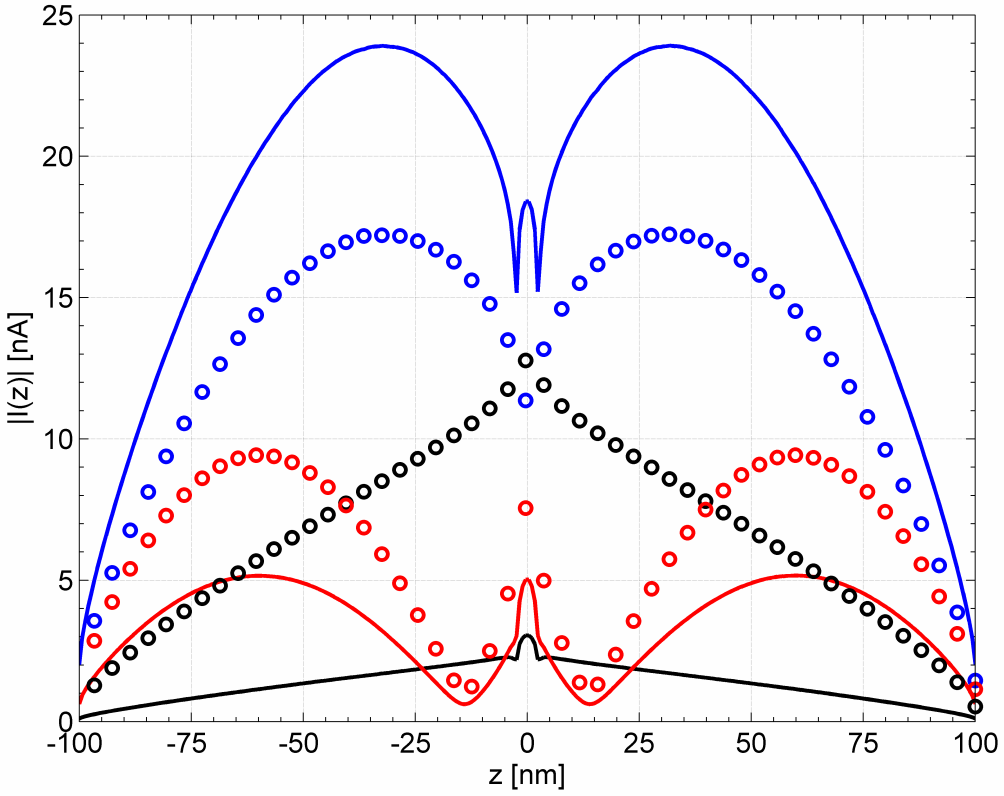

Fig. 4-10: Total current magnitude along a silver, L = 200 nm, a = 5 nm, g = 5 nm nanodipole. Black corresponds to f = 100 THz, blue to f = 200 THz, and red to f = 300 THz. Solid lines are from full discretization while circles are from surface impedance.

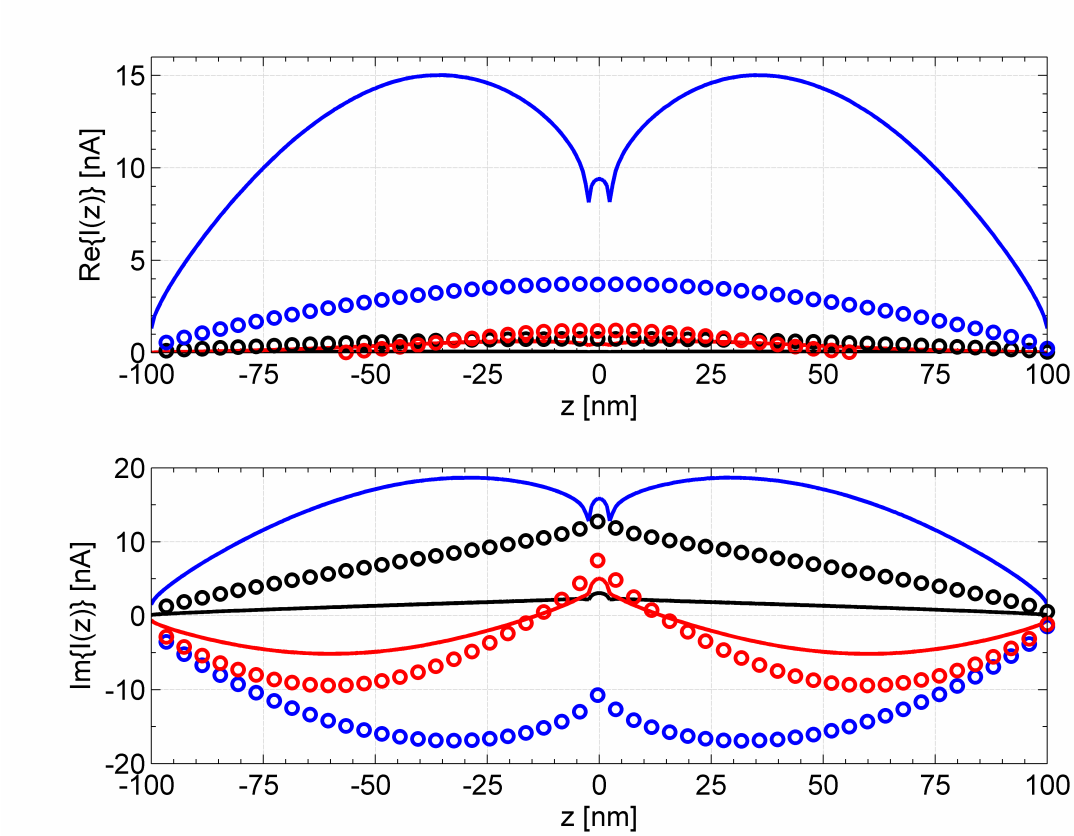

Fig. 4-11: Real and imaginary current flow along a silver, L = 200 nm, a = 5 nm, g = 5 nm nanodipole. Black corresponds to f = 100 THz, blue to f = 200 THz, and red to f = 300 THz. Solid lines are from full discretization while circles are from surface impedance.

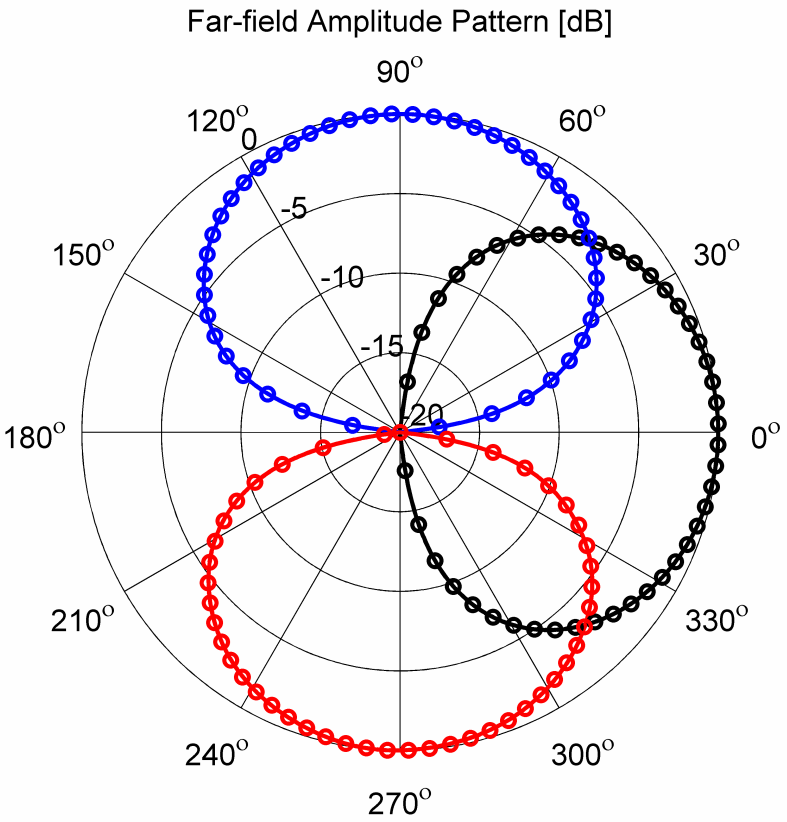

Fig. 4-12: Normalized far-field amplitude pattern for silver, L = 200 nm, a = 5 nm, g = 5nm silver nanodipoles. Black corresponds to f = 100 THz, blue to f = 200 THz, and red to f = 300 THz. Solid lines are from full discretization while circles are from surface impedance. Note that the patterns are rotated away from broadside for clarity.

The calculation of far field quantities requires integration which generally reduces sensitivity to error. Input impedance depends directly on the current and, therefore, is more sensitive to error.

It is important to remember that the surface impedance formulation is an approximation similar to the asymptotic expressions in Chapter 2. We therefore expect to sacrifice some accuracy for the sake of simplicity and speed. Details of the decrease in unknowns, memory, and CPU time are given in Table 4-7. Though this information is given for a specific (and rather small) case, the acceleration is likely even more drastic when considering larger problem sizes.

Table 4-7: Computation details for 301 point frequency sweep with a 2.66 GHz Intel Xeon processor.

	Unknowns	CPU time [s]	Memory [MB]
Full Discretization	83316	2124	1210
Surface Impedance	24382	563	547

4.6 Summary

Optical nanoantennas composed of several different materials were simulated between 100 and 700 THz. In general, the nanoantennas reach impedance resonances corresponding to half-integer multiples of an effective wavelength. This effective wavelength scales based on the nanoantenna geometry and frequency-dependent material parameters. The radiation efficiency of nanoantennas is significantly less than their RF counterparts though this may be improved by judicious selection of radius, material and resonant frequency. Radiation patterns and directivities at the first two resonant frequencies correspond closely to electrically short dipoles because of optical wavelength

scaling. A surface impedance condition may be used to accelerate the computation of antenna parameters, albeit with reduced accuracy in calculating the current distribution, especially the imaginary part. The discrepancy in the current distribution has little effect on far-field quantities due to the inherent integration involved.

Chapter 5

Conclusions

5.1 Summary

We have examined several topics in the area of nanoscale electromagnetics. A key theme has been that most real materials have complex, frequency-dependent dielectric functions at optical frequencies. This requires the reevaluation of usual assumptions about the perfect dielectric or conducting properties inherent in electromagnetic boundary value problems. The ratio of internal intensities within semiconducting nanowires points to an angular dependence in Raman scattering. This ratio is significant even as the nanowire radius becomes infinitesimal. Arrays of nanowires may be used as frequency selective surfaces in the infrared. They also produce intense near fields at optical frequencies, which is of interest in field-enhanced spectroscopy. By introducing excitations, nanowires may operate as optical nanoantennas and, therefore, can be characterized in terms of conventional antenna parameters. Though the efficiency is generally low when compared with conventional RF antennas, they still display directive radiation patterns and optical resonances with reasonable input impedance. A surface impedance approximation reduces the computation time and memory required when simulating dispersive materials of varying conductivity. This approximation properly calculates far field quantities and input resistance, though the input reactance is not evaluated as accurately.

5.2 Future Work

There are still several frontiers that must be explored if optical nanoantennas are to become feasible. A more physical feed model should be implemented. This feed should correspond to actual excitations in optical systems. Through either brute-force computation or numerical efficiency, multiple nanoantenna elements need to be simulated. This will aid in the design of, say, optical Yagi-Uda arrays, where mutual coupling between elements plays an important role. Due to the conductivity roll off in real metals, there may be an upper limit on the attainable resonant frequency with nanoantennas and their efficiency. A further investigation into a wider range of materials may help to clarify this. Also, the actual optical parameters of the material may differ from those in bulk. This requires either direct experimental data or a specific model of the shape dependence.

References

[1] N. Engheta, Alessandro Salandrino, and Andrea Alù, "Circuit Elements at Optical Frequencies: Nanoinductors, Nanocapacitors, and Nanoresistors," *Phys. Rev. Lett.*, vol. 95, pp. 095504:1-4, August 2005.

[2] L. Cao, B. Nabet, and J.E. Spanier, "Enhanced Raman Scattering from Individual Semiconductor Nanocones and Nanowires," *Phys. Rev. Lett.*, vol. 96, pp. 157402:1-4, April 2006.

[3] Q. Xiong, G. Chen, H.R. Gutierrez, and P.C. Eklund, "Raman scattering studies of individual polar semiconducting nanowires: phonon splitting and antenna effects," *Appl. Phys. A*, vol. 85, pp. 299-305, 2006.

[4] Q. Xiong, "Shape Dependence of Physical Properties of Polar Semiconducting Nanowires." Ph.D. diss., Penn State University, 2006.

[5] G. Chen, J. Wu, Q. Lu, H.R. Gutierrez, Q. Xiong, M.E. Pellen, J.S. Petko, D.H. Werner, and P.C. Eklund, "Optical Antenna Effect in Semiconducting Nanowires," *Nano Lett.*, vol. 8, no. 5, pp. 1341-1346, April 2008.

[6] G.W. Hanson, "On the Applicability of the Surface Impedance Integral Equation for Optical and Near Infrared Copper Dipole Antennas," *IEEE Trans. Antennas Propag.*, vol. 54, no. 12, pp. 3677-3685, December 2006.

[7] C.F. Bohren and D.R. Huffman, *Absorption and Scattering of Light by Small Particles.* New York: Wiley, 1983.

[8] P.B. Johnson and R.W. Christy, "Optical Constants of the Noble Metals," *Phys. Rev. B*, vol. 6, no. 12, pp. 4370-4379, December 1972.

[9] R. T. Kinasewitz and B. Senitzky, "Investigation of the complex permittivity of *n*-type silicon at millimeter wavelengths," *J. Appl. Phys.*, vol. 54, no. 6, pp. 3394-3398, June 1983.

[10] A.D. Rakić, A.B. Djurišić, J.M. Elazer, and M.L. Majewski, "Optical properties of metallic films for vertical-cavity optoelectronic devices," *Appl. Opt.*, vol. 37, no. 22, pp. 5271-5283, August 1998.

[11] I. Puscasu, W.L. Schiach, and G.D. Boreman, "Modeling parameters for the spectral behavior of infrared frequency selective surfaces," *Appl. Opt.*, vol. 40, no. 1, pp. 118-124, January 2001.

[12] W.L. Puscasu, G.D. Boreman, *et al*., "Optical resonances in periodic surface arrays of metallic patches," *Appl. Opt.*, vol. 42, no. 28, pp. 5714-5721, October 2003.

[13] B. Monacelli, B.A. Munk, G.D. Boreman, *et al*., "Infrared Frequency Selective Surface Based on Circuit-Analog Square Loop Design," *IEEE Trans. Antennas Propag.*, vol. 53, no. 2, pp. 745-752, February 2005.

[14] J.A. Bossard, D.H. Werner, T.S. Mayer, J.A. Smith, Y.U. Tang, R.P. Drupp, and L. Li, "The Design and Fabrication of Planar Multiband Metalllodielectric Frequency Selective Surfaces for Infrared Applications," *IEEE Trans. Antennas Propag.*, vol. 54, no. 4, pp. 1265-1276, April 2006.

[15] K.B. Crozier, A. Sundaramurthy, G.S. Kino, and C.F. Quate, "Optical antennas: Resonators for local field enhancement," *J. Appl. Phys.*, vol. 94, no. 7, pp. 4632-4642, October 2003.

[16] A. Sundaramurthy, K.B. Crozier, G.S. Kino, D.P. Fromm, P.J. Schuck, and W.E. Moerner, "Field enhancement and gap-dependent resonance in a system of two opposing tip-to-tip Au nanotriangles," *Phys. Rev. B*, vol. 72, pp. 165409: 1-6, October 2005.

[17] J. Aizpuruam G.W. Bryant, L.J. Richter, and F.J. García de Abajo, "Optical properties of coupled metallic nanorods for field-enhanced spectroscopy," *Phys. Rev. B*, vol. 71, pp. 235420: 1-13, June 2005.

[18] C.J. Orendorff, L. Gearheart, N.R. Jana, and C.J. Murphy, "Aspect ratio dependence on surface enhanced Raman scattering using silver and gold nanorod substrates," *Phys. Chem. Chem. Phys.*, vol. 8, pp. 165-170, 2006.

[19] E.J. Smythe, E. Cubukcu, and F. Capasso, "Optical properties of surface plasmon resonances of coupled metallic nanorods," *Opt. Express*, vol. 15, no. 12, pp. 7439-7447, June 2007.

[20] K. Kneipp, M. Moskovits, and H. Kneipp, eds. *Surface-Enhanced Raman Scattering: Physics and Applications*. Berlin, Germany: Springer, 2006.

[21] P. Mühlschlegel, H.-J. Eisler, O.J.F. Martin, B. Hecht, and D.W. Pohl, "Resonant Optical Antennas," *Science*, vol. 308, pp. 1607-1608, June 2005.

[22] J. Li, A. Salandrino, and N. Engheta, "Shaping the Beam of Light in Nanometer Scales: A Yagi-Uda Nanantenna in the Optical Domain," *under review*: arXiv:cond-mat/0703086v1, submitted: March, 2007.

[23] T.H. Taminiau, F.B. Segerink, and N.F. van Hulst, "A Monopole Antenna at Optical Frequencies: Single-Molecule Near-Field Measurements," *IEEE Trans. Antennas Propag.*, vol. 55, no. 11, pp. 3010-3017, November 2007.

[24] M.E. Pellen, M.G. Bray, J.S. Petko, D.H. Werner, Q. Xiong, G. Chen, and P.C. Eklund, "Electromagnetic Scattering from Long Nanowires," *2007 IEEE Antennas Propag. Int. Symp.*, Honolulu, HI, pp. 3392-3395, June 2007.

[25] R.F. Harrington, *Time-Harmonic Electromagnetic Fields*. Piscataway, NJ: IEEE Press, 2001.

[26] C.A. Balanis, *Advanced Engineering Electromagnetics*. New York: Wiley, 1989.

[27] M.E. Pellen, *Electromagnetic Modeling of Nanowires at Infrared and Optical Wavelengths*, Master's thesis, Penn State University, 2008.

[28] A. Pucci, *et al*, "Resonances of individual metal nanowires in the infrared," *Appl. Phys. Lett.*, vol 89, no. 253104, pp. 1-3, December 2006.

[29] L. Novotny, "Effective Wavelength Scaling for Optical Antennas," *Phys. Rev. Lett.*, vol. 98, no. 266802, pp. 1-4, June 2007.

[30] G.W. Bryant, F.J. García de Abajo, and J. Aizpurua, "Mapping the Plasmon Resonances of Metallics Nanoantennas," *Nano Lett*., vol. 8, no. 2, pp. 631-636, February 2008.

[31] T.F. Eibert, J.L. Volakis, D.R. Wilton, and D.R. Jackson, "Hybrid FE/BI Modeling of 3-D Doubly Periodic Structures Utilizing Triangular Prismatic Elements and an MPIE Formulation Accelerated by the Ewald Transform," *IEEE Trans. Antennas Propag.*, vol 47, no. 5, pp. 843-850, May 1999.

[32] C.A. Balanis, *Antenna Theory: Analysis and Design.* New York: Wiley, 2005.

[33] J. Alda, J.M. Rico-García, J.M. López-Alonso, and G Boreman, "Optical antennas for nano-photonic applications," *Nanotechnology*, vol. 16, pp.S230-S234, March 2005.

[34] D.W. Pohl, "Near Field Optics Seen as an Antenna Problem," *The Second Asia Pacific Workshop on Near Field Optics*, Beijing, China, pp. 9-21, October, 1999.

[35] H.F. Hofmann, T. Kosako, and Y. Kadoya, "Design parameters for a nano-optical Yagi-Uda antenna," *New J. Phys.*, vol. 9, no. 217, pp. 1-12, July 2007.

[36] J. Li, and N. Engheta, "Core-Shell Nanowire Optical Antennas Fed by Slab Waveguides," *IEEE Trans. Antennas Propag.*, vol.55, no. 11, pp. 3018-3026, November, 2007.

Appendix

Derivation of Surface Impedance for a Solid Cylindrical Wire

Maxwell's equations in cylindrical coordinates and a source-free region are

$$\begin{aligned} \frac{1}{\rho}\frac{\partial H_z}{\partial \varphi} - \frac{\partial H_\varphi}{\partial z} &= j\omega\varepsilon E_\rho & \frac{1}{\rho}\frac{\partial E_z}{\partial \varphi} - \frac{\partial E_\varphi}{\partial z} &= -j\omega\mu H_\rho \\ \frac{\partial H_\rho}{\partial z} - \frac{\partial H_z}{\partial \rho} &= j\omega\varepsilon E_\varphi & \frac{\partial E_\rho}{\partial z} - \frac{\partial E_z}{\partial \rho} &= -j\omega\mu H_\varphi \\ \frac{\partial(\rho H_\varphi)}{\partial \rho} - \frac{\partial H_\rho}{\partial \varphi} &= j\omega\varepsilon(\rho E_z) & \frac{\partial(\rho E_\varphi)}{\partial \rho} - \frac{\partial E_\rho}{\partial \varphi} &= -j\omega\mu(\rho H_z) \end{aligned} \qquad \text{(A-1)}$$

where μ and ε are the usual constitutive parameters of the medium.

An infinite cylindrical wire will support no field variation in φ or z. Therefore, (A-1) reduces to

$$\begin{aligned} \frac{\partial H_z}{\partial \rho} &= -j\omega\varepsilon E_\varphi & \frac{\partial E_z}{\partial \rho} &= j\omega\mu H_\varphi \\ \frac{\partial(\rho H_\varphi)}{\partial \rho} &= j\omega\varepsilon(\rho E_z) & \frac{\partial(\rho E_\varphi)}{\partial \rho} &= -j\omega\mu(\rho H_z) \end{aligned} \qquad \text{(A-2)}$$

These two sets of equations give rise to two orthogonal sets of waves, *transverse magnetic* (TM) and *transverse electric* (TE). The wire will support TM waves, which have only the field components E_z and H_φ. Combining the two coupled differential equations,

$$\frac{\partial(\rho H_\varphi)}{\partial \rho} = j\omega\varepsilon(\rho E_z) \qquad \frac{\partial E_z}{\partial \rho} = j\omega\mu H_\varphi \qquad \text{(A-3)}$$

results in a wave equation in E_z,

$$\frac{\partial^2 E_z}{\partial \rho^2} + \frac{1}{\rho}\frac{\partial E_z}{\partial \rho} + k^2 E_z = 0 \tag{A-4}$$

where k^2 is generally a complex number. Rearranging to

$$\frac{\partial^2 E_z}{\partial (jk\rho)^2} + \frac{1}{jk\rho}\frac{\partial E_z}{\partial (jk\rho)} - E_z = 0 \tag{A-5}$$

gives a *modified Bessel equation* of the zeroth order. The solutions *within* the wire are

$$E_z = AI_0(jk\rho) + BK_0(jk\rho) \tag{A-6}$$

To avoid a singularity at $\rho = 0$, the coefficient B must vanish. The magnetic field can be found from (A-3)

$$H_\varphi = \frac{kA}{\omega\mu} I_0'(jk\rho) \tag{A-7}$$

The surface impedance is defined as the ratio of electric and magnetic fields at the material surface ($\rho = a$ in this case)

$$Z_s \triangleq \frac{E_z|_{\rho=a}}{H_\varphi|_{\rho=a}} = \frac{k}{\omega\mu}\frac{I_0(jka)}{I_0'(jka)} \tag{A-8}$$

Introducing the intrinsic impedance of free space, η_0, and the relative permittivity of the material, ε_r, this becomes

$$Z_s = \frac{\eta_0}{\sqrt{\varepsilon_r}}\frac{I_0(jka)}{I_1(jka)} \tag{A-9}$$

where the recurrence relation

$$I_0'(x) = I_1(x) \tag{A-10}$$

was also used.